# Velocity and geometry of propagating fronts in complex convective flow fields

S. Mukherjee

*Department of Biomedical Engineering and Mechanics, Virginia Tech, Blacksburg, Virginia 24061, USA*

M. R. Paul[*]

*Department of Mechanical Engineering, Virginia Tech, Blacksburg, Virginia 24061, USA*

We numerically study the propagation of reacting fronts through three-dimensional flow fields composed of convection rolls that include time-independent cellular flow, spatiotemporally chaotic flow, and weakly turbulent flow. We quantify the asymptotic front velocity and determine its scaling with system parameters including the local angle of the convection rolls relative to the direction of front propagation. For cellular flow fields, the orientation of the convection rolls has a significant effect upon the front velocity and the front geometry remains relatively smooth. However, for chaotic and weakly turbulent flow fields, the front velocity depends upon the geometric complexity of the wrinkled front interface and does not depend significantly upon the local orientation of the convection rolls. Using the box counting dimension we find that the front interface is fractal for chaotic and weakly turbulent flows with a dimension that increases with flow complexity.

## I. INTRODUCTION

Reacting fronts that propagate in the presence of complex three-dimensional fluid flows are ubiquitous with many implications in science, nature, and technology [1,2]. An improved fundamental understanding of propagating fronts in complex fluid flows would have a direct impact upon a number of important challenges that face us today. Examples include the combustion of premixed gases in the turbulent flow that occurs in an internal combustion engine [3–7], the complex patterns of reagents that occur in many chemical industrial processes [1,2,8–10], the spread of a forest fire [11–13], the spatiotemporal dynamics of a species invasion [14], and the outbreak of an epidemic such as the flu in a moving population [15,16].

In these situations, the propagating front can often be modeled as a reaction that consumes unreacted species (the unstable phase) in its path while leaving behind only products (the stable phase). The front dynamics and geometry are highly nonlinear and depend strongly on the underlying flow field dynamics.

There has been significant effort studying the dynamics and geometry of propagating fronts in the presence of fluid motion (cf. [1,2]). This has received intense interest in the area of combustion in a turbulent flow field [4,17]. In addition, there has been a broad range of work on propagating fronts for flow fields that are not turbulent. Examples include the study of fronts in a shaken layer of liquid exhibiting Faraday waves [18], convective flows [19–21], Hele-Shaw flows [22], Marangoni flows [23], and fields of disordered vortices [24,25], to name a few.

However, the majority of this work has been for fronts in simple or idealized fluid flows such as cellular flows, vortex chains, and vortex arrays. Typically, this allows one to quantify the velocity of the propagating front in terms of system parameters such as the characteristics of the flow field and the details of the nonlinear reaction. In many cases, the front velocity is found to exhibit a power-law scaling with a characteristic velocity of the fluid. For limiting cases, theoretical predictions are available for the scaling exponent (cf. [26,27]).

Here, we explore the more difficult problem of propagating fronts in spatially disordered flows with time dependence. We use large-scale parallel numerical simulations to explore propagating fronts in flow fields over the range of cellular flow, chaotic flow, and weakly turbulent flow for a three-dimensional layer of fluid for the precise conditions of the laboratory. In order to generate these flow fields, we use Rayleigh-Bénard convection which is the buoyancy driven fluid motion of a layer of fluid [28]. Our findings for the front velocity are also captured by the power-law scaling ideas that describe idealized flows and we connect our results with theoretical predictions where possible.

The geometry of a propagating front is well known to significantly affect the dynamics of the front (cf. [4,18,24,29,30]). The more wrinkled and intricate the front is, the larger the interfacial region between the products and reactants that is available for the reaction to occur. One well known mechanism to increase the complexity of the front geometry is through the motion of the underlying flow field. This has received intense interest in the area of combustion in a turbulent flow field [4,17].

An appealing approach to quantify the geometry of the front is to compute its dimension. For many cases of interest, the geometry of the front has been shown to be a fractal and even multifractal [17,31,32]. An interesting feature that has

---

[*]Corresponding author: mrp@vt.edu

emerged is the finding that the fractal dimension of the front $D_f$ is found to be $D_f \approx \frac{7}{3}$ for a wide variety of conditions and flow fields [4,18,33,34].

There have been theoretical ideas presented [4,33] that predict $D_f = \frac{7}{3}$, however, these theories rely upon the specific features and scaling of homogeneous turbulent flows. It has also been shown numerically [35] that the transport of a passive scalar in a chaotic flow field can exhibit fractal (and even multifractal) behavior without the presence of small-scale fluid structures.

We also compute the dimension of propagating fronts in chaotic and weakly turbulent flows. Our results yield fractional values for the dimension of the front. We explore how the dimension varies with properties of the flow field to help build our understanding of fronts in complex flow fields.

Propagating fronts in chaotic Rayleigh-Bénard convection have been studied in Ref. [20]. This study focused upon the spiral defect chaos state in an advection dominated regime. Using a measure of the mean squared displacement of the front, or front spreading, it was shown that the chaotic flow field enhanced the front propagation. Furthermore, using a measure of the front area it was found that the geometry of the fronts become more complex with increasing flow field complexity.

In this paper, we have probed these issues much further by computing the front velocity and dimension for a wide range of parameters and flow fields. In our study we have undertaken a methodical approach by exploring several flow fields of increasing complexity. We investigate time-independent cellular flow, chaotic flow, and weakly turbulent flow. In all cases, the main characteristic of the flow field is that it is composed of convection rolls of increasing complexity. We first study propagating fronts through a field of straight and parallel convection rolls which includes quantifying the fronts propagating at an angle relative to the convection rolls. We then use these insights to guide our study of propagating fronts in chaotic and weakly turbulent flow fields which are composed of dynamic patches of convection rolls at various orientations that are separated by many defect structures. Overall, we use our results to build a better physical understanding of the front dynamics and geometry for fronts traveling through complex three-dimensional convective flow fields.

The paper is organized as follows. In Sec. II we discuss our overall approach. We present the governing equations for Rayleigh-Bénard convection and the reaction-advection-diffusion equation and provide some details regarding our computational approach. In Sec. III we discuss the results of our numerical exploration. We describe the velocity of the propagating fronts for no flow, straight-parallel convection rolls, and then chaotic and weakly turbulent flow. We then explore the geometry of the propagating front for these conditions. Lastly, in Sec. IV we present some concluding remarks.

## II. APPROACH

### A. Fluid equations

An integral component of our study is the ability to quantify front propagation in a range of three-dimensional flow fields of varying complexity. In order to accomplish this,

we use the canonical pattern forming system of Rayleigh-Bénard convection [28] to create time-independent, chaotic, and weakly turbulent flow fields.

Rayleigh-Bénard convection is the fluid motion that occurs when a shallow layer of fluid is heated uniformly from below in a gravitational field. The fluid motion is governed by the nondimensional Boussinesq equations

$$\mathrm{Pr}^{-1}\left(\frac{\partial \vec{u}}{\partial t} + \vec{u} \cdot \vec{\nabla}\vec{u}\right) = -\vec{\nabla}p + \nabla^2\vec{u} + \mathrm{Ra}T\hat{z}, \quad (1)$$

$$\frac{\partial T}{\partial t} + \vec{u} \cdot \vec{\nabla}T = \nabla^2 T, \quad (2)$$

$$\vec{\nabla} \cdot \vec{u} = 0 \quad (3)$$

which represent the conservation of momentum, energy, and mass. In our notation, $\vec{u}(x, y, z, t) = (u, v, w)$ is the fluid velocity vector with components $(u, v, w)$ in the $(x, y, z)$ directions, respectively. $T(x, y, z, t)$ is the temperature, $p(x, y, z, t)$ is the pressure, $t$ is time, and $\hat{z}$ is a unit vector opposing gravity.

These equations have been nondimensionalized in the typical manner (cf. [36]) using the depth $d$ of the convection layer as the length scale, the constant temperature difference between the hot bottom surface and the cold top surface $\Delta T$ as the temperature scale, and the thermal diffusion time $d^2/\alpha$ across the layer depth as the timescale where $\alpha$ is the thermal diffusivity of the fluid.

The Rayleigh number $\mathrm{Ra} = \beta g \Delta T d^3/(\alpha\nu)$ is the ratio of buoyancy to dissipation where $\beta$ is the coefficient of thermal expansion, $g$ is the acceleration due to gravity, and $\nu$ is the kinematic viscosity of the fluid. For an infinite layer of fluid, the critical value of the Rayleigh number at the onset of convection is $\mathrm{Ra}_c \simeq 1707.76$ [28]. As the Rayleigh number is increased from zero, the fluid will transition from a no-flow state to time-independent convection rolls at $\mathrm{Ra}_c$. Further increases in Ra will result in time-dependent dynamics including periodic dynamics, chaotic dynamics, and eventually turbulence. We will use Ra as the control parameter to vary the complexity of the underlying flow field.

The Prandtl number $\mathrm{Pr} = \nu/\alpha$ is the ratio of the diffusivities of momentum and heat. In our exploration, we will always use $\mathrm{Pr} = 1$ which is aligned with the Prandtl numbers often found in compressed gas convection experiments [37,38].

### B. Reaction-advection-diffusion equation

Although the applications of propagating fronts in complex fluid flows are extremely broad and rich, the physics for many cases of interest can be captured with a general continuum formulation using coupled nonlinear partial differential equations. We use the nondimensional reaction-advection-diffusion equation

$$\frac{\partial c}{\partial t} + \vec{u} \cdot \vec{\nabla}c = \mathrm{Le}\nabla^2 c + \xi f(c), \quad (4)$$

where Le is the Lewis number, to describe the propagating front. We have used the same length and timescales that were used to nondimensionalize Eqs. (1)–(3).

The concentration $c(x, y, z, t)$ is a single scalar quantity that represents the ratio of products to reactants where

$c = 1$ is pure products (no reactants), $c = 0$ is pure reactants (no products), and intervening values $0 < c < 1$ represent a mixture of products and reactants.

The last term on the right side of Eq. (4) is the production term that describes the reaction where $\xi$ is the nondimensional reaction rate. In our computations we use the Fischer-Kolmogorov-Petrovskii-Piskunov (FKPP) nonlinearity [39,40] where $f(c) = c(1 - c)$. This quadratic nonlinearity is commonly used to model a wide range of reacting processes [1]. For these types of reactions, the production is proportional to the concentration of products $c$ and to the concentration of reactants $(1 - c)$.

It will be important in our upcoming discussions to clearly define how we will describe the propagating fronts. For the FKPP nonlinearity, a reaction will occur anywhere in the flow field where $0 < c < 1$. In all of the problems we explore, the region where the reaction is occurring is not a sharp feature and the reaction occurs over a distributed region of space. We will define the *reaction zone* as the region of space where $0.1 \leqslant c \leqslant 0.9$. We will refer to the width of this region as the reaction zone thickness $\delta$. We will define the *front* as the level-set contour of the concentration field $c$ at maximum production. For the FKPP nonlinearity, the maximum production occurs at $c = \frac{1}{2}$. Therefore, the front is the surface that results from the level-set contour of $c = \frac{1}{2}$.

In the discussions that follow, we will clearly state the boundary and initial conditions for each particular situation of interest. However, they fall into the following general categories. We use the no-slip boundary condition $\vec{u} = 0$ at all material surfaces that are in contact with the fluid. In some cases, where we have removed the walls, we instead use periodic boundary conditions for the fluid velocity. The temperature of the bottom and top surfaces are always held constant, where the bottom surface is hot $T(z = 0) = 1$ and the top surface is cold $T(z = 1) = 0$. The thermal boundary conditions for the sidewalls are either perfectly conducting, periodic, or hot depending upon the particular problem of interest. For the concentration field $c$, all material walls are treated as no-flux surfaces. In some cases we have used periodic boundary conditions for the concentration as needed.

The initial conditions for the flow field are small random perturbations to the temperature field. The simulations are then evolved for a long time to ensure that all initial transients have decayed to yield the flow field of interest such as straight-parallel convection rolls or chaotic dynamics. The reaction is initiated by supplying an initial spatial variation to the concentration field $c(x, y, z, t_0)$ where $t_0$ is the time when the reaction starts. All of our initial conditions are chosen to be sufficiently steep in order to yield pulled propagating fronts [1].

We use a highly efficient, parallel, and spectral-element approach to numerically integrate the coupled equations given by Eqs. (1)–(3) and (4). We use the open source solver NEK5000 [41,42]. The computations are third-order accurate in time and exponentially convergent in space. For more details describing the use of this approach for Rayleigh-Bénard convection, see Ref. [36] and for a discussion of computations of passive scalar transport and propagating fronts using this approach, see Refs. [20,43].

The Lewis number Le is the ratio of mass diffusion to heat diffusion $Le = D/\alpha$ where $D$ is the mass diffusivity

of the reactants and products. The flow field will have a stronger effect upon the front dynamics as the Lewis number is decreased. Using our scaling, the nondimensional timescale for mass diffusion can be expressed as $\tau_D = Le^{-1}$.

Although the Damköhler number Da and the Péclet number do not appear explicitly in Eqs. (1)–(3) and (4) we will find these nondimensional numbers useful in our discussion. The Damköhler number can be expressed as the ratio of the nondimensional fluid flow field timescale $\tau_u$ to the nondimensional reaction timescale $\tau_r$. The flow field timescale is given by $\tau_u = U^{-1}$ where $U$ is the nondimensional characteristic velocity describing the flow field. In fact, using our nondimensionalization the variable $U$ can be thought of as the thermal Péclet number. In our computations, we will use the time average of the maximum value of the fluid velocity magnitude $||\vec{u}||$ as the characteristic velocity. The reaction timescale is given by $\tau_r = \xi^{-1}$. Using these timescales yields $Da = \tau_u/\tau_r = \xi/U$.

When $Da \gg 1$, the dynamics is reaction dominated and the reaction zone thickness $\delta$ is very thin compared to a characteristic length $L$ of the flow field. For our convection flow fields we will use the width of a convection roll as the characteristic length scale where $L \sim O(1)$.

In the special limit $Da \gg 1$ where $Le \to 0$ and $\tau_r \to 0$ while $Le/\tau_r$ remains constant, one reaches the geometric optics limit. This yields a reaction zone with a finite speed and zero thickness [2]. This particular limit is very attractive theoretically, however, we do not explore this limit in our calculations and focus our attention on finite sized reaction zones with finite speeds of propagation.

Lastly, when $Da \ll 1$, the dynamics is advection dominated which yields a distributed reaction zone. In our investigation, we have focused upon the regime where $0.1 \lesssim Da \lesssim 1$ which yields reaction zones of finite thickness that are affected significantly by the underlying flow field.

The Péclet number $Pe = U/Le$ is the ratio of convection to mass diffusion. In our results we explore the range $0 \leqslant Pe \lesssim 10^3$ which spans dynamics without fluid flow to dynamics where the flow field is significant.

We emphasize that in Eqs. (1)–(3) and (4) the dynamics of the flow field ($\vec{u}$, $p$, and $T$) is not affected by the dynamics of the concentration field $c$. In other words, we have not included the *back-action* from the reaction onto the flow field. In many systems, such as nonexothermic chemical, fluid, or biological systems, this additional coupling is not necessary. A fundamental understanding of the front dynamics without the back-action is an essential first step and will have a direct impact upon important problems of broad appeal. This is the focus of what we discuss here.

However, our numerical approach is quite general and this restriction could be removed to allow a study of the complex interactions that would result from back-action. This is beyond the scope of this work and is a topic of future interest.

## III. RESULTS AND DISCUSSION

The parameter space describing propagating fronts in fluid flows is vast with many interesting limits and specific cases of fundamental importance. In addition, the parallel computations are often expensive and care was needed in deciding

how to proceed. Our approach is motivated by imagining the following experiment. We assume that the fluid properties and the nonlinear reaction are set and that we want to study how a propagating front is affected by flow fields of differing complexity by varying only the Rayleigh number. In this study, we explore the range $0 \leqslant \mathrm{Ra} \leqslant 25\,000$ for several different geometries and configurations for the convective domain.

Furthermore, we explore two different classes of convective flow fields: (i) a flow field of time-independent straight-parallel convection rolls (a cellular flow); and (ii) a chaotic or weakly turbulent flow field composed of rapidly varying convection rolls and defect structures. We will take advantage of the fact that for some cases both (i) and (ii) are possible numerically for the same value of Ra. In our discussion, we will find the insights from (i) very useful for building a physical understanding of (ii).

We focus our investigation on two different fluids where the molecular diffusion of one fluid, with Le = 1, is an order of magnitude larger than that of the other with Le = 0.1. In all of our simulations, we hold the Prandtl number constant at Pr = 1 and, unless stated otherwise, we keep the reaction rate constant at $\xi = 9$. These choices allow us to explore the dynamics of propagating fronts for $0 \leqslant \mathrm{Pe} \lesssim 1000$ and $0.1 \lesssim \mathrm{Da} \lesssim 30$.

### A. Velocity of a propagating front

We first quantify the propagating front in the absence of a flow field. We use this to establish our approach for computing front velocities while quantifying important baseline properties. Next, we investigate the dynamics of a propagating front in a field of straight and parallel convection rolls where we vary the characteristic velocity $U$ of the convection rolls. Lastly, we compute the velocity of propagating fronts in chaotic and weakly turbulent flow fields using a large cylindrical convection domain.

In the absence of fluid motion where $\vec{u} = 0$ it is well known [1,39,40] that the long-time asymptotic front velocity is given by the constant value

$$v_0 = 2\sqrt{\mathrm{Le}\xi}. \tag{5}$$

A measure of the reaction zone thickness, or width, can be expressed as [27,40]

$$\delta_0 = 8\sqrt{\frac{\mathrm{Le}}{\xi}}. \tag{6}$$

The reaction zone thickness predicted by Eq. (6) describes the length scale where $0.1 \lesssim c \lesssim 0.9$. This corresponds with the range of concentration values $0.1 \leqslant c \leqslant 0.9$ that we will use to quantify the reaction zones present in our numerical results. Using our nondimensionalization, a length of unity is the depth of the fluid layer which is also approximately equal to the width of a single convection roll.

We first consider the box shaped domain shown in Fig. 1 with depth $d$ and side lengths $L_x$ and $L_y$ in the $x$ and $y$ directions, respectively. For this domain, its size is described using the two aspect ratios $\Gamma_x = L_x/d$ and $\Gamma_y = L_y/d$ where we have chosen $\Gamma_x = 30$ and $\Gamma_y = 5$. The domain is filled with a quiescent fluid such that $\vec{u} = 0$ and $\mathrm{Ra} < \mathrm{Ra}_c$. The top ($z = 1$)
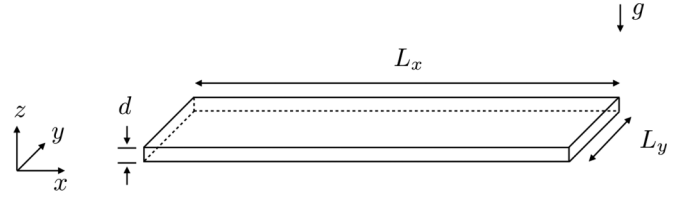


FIG. 1. A schematic of the rectangular domain. The Cartesian coordinates $(x, y, z)$ are as shown with the origin at the lower left corner of the domain where $z$ is opposing the direction of gravity $g$. The length of the domain is $L_x$ and $L_y$ in the $x$ and $y$ directions, respectively, and the depth of the fluid layer is $d$. The aspect ratios are $\Gamma_x = L_x/d = 30$ and $\Gamma_y = L_y/d = 5$ (figure is drawn to scale).

and bottom ($z = 0$) surfaces, as well as the sidewalls at the far left ($x = 0$) and right ($x = 30$), are solid surfaces with no-flux boundary conditions $\vec{\nabla} c \cdot \hat{n} = 0$ where $\hat{n}$ is an outward pointing unit normal. The domain has periodic boundary conditions on all field variables in the $y$ direction. This is, essentially, a two-dimensional computation since there is no variation in the $y$ direction. However, we will find it useful to treat this numerically as the full three-dimensional problem for clarity of visualization and for comparison with our computations where this symmetry is broken.

To initiate the reaction at time $t_0$, the concentration field is set to $c(x, y, z, t_0) = e^{-\lambda x}$. The steepness of the initial condition is determined by $\lambda$, when $\lambda \geqslant \lambda^*$ the resulting front will be a pulled front [1]. For our problem $\lambda^* = v_0/(2\mathrm{Le})$ and we have always used $\lambda > \lambda^*$ in our simulations to generate pulled fronts that propagate from left to right.

We are interested in studying reaction zones of finite thickness that may have a complex spatial and temporal dependence. As a result, the determination of the instantaneous front velocity $v_f(t)$ must be handled with some care. We will use the idea of the bulk burning rate [44] as one way to compute the front velocity. For a propagating front traveling in the positive $x$ direction, this can be expressed as

$$v_f(t) = \int_0^1 dz \int_0^{\Gamma_x} dx \frac{\partial c}{\partial t}. \tag{7}$$

This definition of the front velocity has been shown to be mathematically and physically reasonable for a variety of general situations [26,27,44]. Equation (7) correctly quantifies the velocity of traveling wave solutions while also capturing the velocity of fronts in more complicated situations where such solutions may not exist and it does not require any assumptions about the reacting region [44]. Furthermore, the approach extends in a straightforward manner to the complex fronts we will discuss shortly.

A further complication is that the velocity $v_f(t)$ of pulled fronts slowly approach their long-time asymptotic values $\bar{v}_f$ where $\bar{v}_f = \lim_{t \to \infty} v_f(t)$. This slow convergence is universal and scales algebraically as $O(t^{-1})$ [45]. In light of this, we use the equation

$$v_f(t) = \bar{v}_f - \frac{b}{t} \tag{8}$$

to determine values of $\bar{v}_f$ from our finite-time data for $v_f(t)$. This is of direct importance to our study, in part, because it
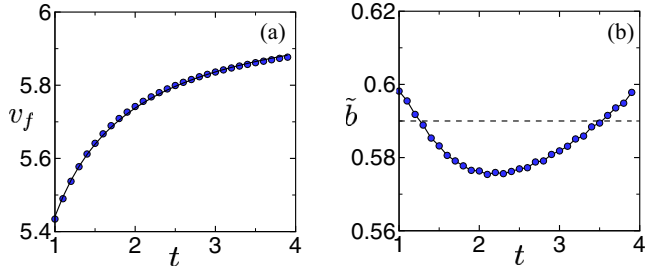
FIG. 2. (a) The time variation of the front velocity $v_f(t)$ for the case of a quiescent fluid with Le = 1, $\xi = 9$ and using the rectangular geometry shown in Fig. 1. The front was initiated at the left wall and propagates to the right. $v_f(t)$ is computed using Eq. (7). The solid line is a curve fit using Eq. (8) which yields $\bar{v}_f = 6.03$ and $b = 0.59$. For these conditions, $v_0 = 6$ as given by Eq. (5). (b) The time variation of $\tilde{b}$ where $\tilde{b} = t[\bar{v}_f - v_f(t)]$. The dashed line represents the value $b = 0.59$ that is determined from the curve fit shown in (a).

determines how large the spatial extent of our fluid domains need to be in order to determine a value of the asymptotic front velocity $\bar{v}_f$.

Figure 2(a) shows representative numerical results for a propagating front for a fluid with Le = 1 in a container with no fluid motion $\vec{u} = 0$. The symbols represent numerical values of $v_f(t)$ computed using Eq. (7). The solid line is a curve fit through the data using Eq. (8) which is used to determine the long-time value of the front speed $\bar{v}_f$.

For these conditions, the theoretical value of the front speed is $v_0 = 6$ and our numerical simulation yields $\bar{v}_f = 6.03$ which is in excellent agreement. For times $t \gtrsim 5$ the sidewall on the right hand side of the domain affects the front dynamics and therefore we do not include this in our estimate for $\bar{v}_f$. These results also suggest that a domain with $\Gamma_x \gtrsim 30$ is sufficiently large for us to compute $\bar{v}_f$ in this parameter regime.

For a front traveling in the absence of a fluid flow, the front can be identified as the location in the $x$ direction where $c = \frac{1}{2}$, which is independent of $z$. The front velocity can then be determined as the time rate of change of the front location. Computing a front velocity in this manner for our numerical results yields an asymptotic front velocity of $\bar{v}_f = 5.99$.

To check the consistency of using Eq. (8) to curve fit the data, we show in Fig. 2(b) the variation of $\tilde{b}(t)$ with time $t$ where $\tilde{b}(t) = t[\bar{v}_f - v_f(t)]$. The horizontal dashed line is the value of $b$ determined from the entire curve fit shown in Fig. 2(a) where $b = 0.59$. Figure 2(b) illustrates only a small variation in $\tilde{b}(t)$ with time which suggests that Eq. (8) does capture the time variation of the front velocity. We have not explored further the particular shape of the curve shown in Fig. 2(b). We have validated our approach and computations for a range of parameters to ensure the accuracy of these findings.

### 1. Fronts propagating in straight-parallel convection rolls

We next explore propagating fronts in the presence of a flow field composed of straight and parallel convection rolls. We use the box domain shown in Fig. 1 but this time with a
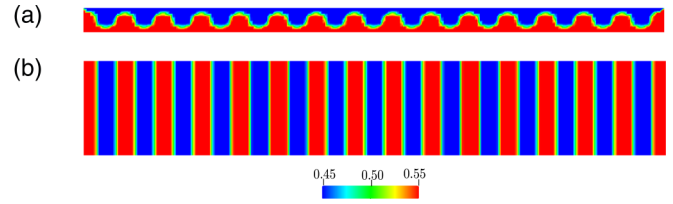


FIG. 3. A cellular flow field composed of straight and parallel convection rolls in a box domain for Ra = 3000 (see Fig. 1). (a) Color contours of the temperature field in the $x$-$z$ plane at $y = \Gamma_y/2$. Red is hot rising fluid and blue is cold falling fluid. (b) Color contours of the temperature field in the $x$-$y$ plane at $z = \frac{1}{2}$. In this panel the location of the center of a convection roll is green and this layer contains 30 counter-rotating convection rolls. The walls at the left and right ends are hot $T(x = 0, y, z, t) = T(x = \Gamma_x, y, z, t) = 1$ which causes the formation of straight-parallel convection rolls. The boundary conditions in the $y$ direction are periodic.

value for the Rayleigh number that is above the critical threshold Ra > $Ra_c$. We again use periodic boundary conditions for all of the field variables in the $y$ direction.

To create a field of time-independent counter-rotating convection rolls that are stacked in the $x$ direction (i.e., with their roll axes pointing in the $y$ direction), we use a hot sidewall boundary condition for the left and right walls such that $T(x = 0, y, z, t) = T(x = \Gamma_x, y, z, t) = 1$. The hot sidewalls cause fluid to rise near the sidewall (for all values of Ra) which initiates the formation of $x$ rolls that propagate inward to fill the entire fluid domain. We continue the simulation until all initial transients have decayed and the result is a field of time-independent convection rolls.

A typical flow field is shown in Fig. 3 for Ra = 3000. The color contours represent the temperature of the fluid where red is hot rising fluid and blue is cold falling fluid. A side view of the flow field is shown in Fig. 3(a) using a $x$-$z$ projection at $y = \Gamma_y/2$. A top view is shown in Fig. 3(b) using a $x$-$y$ projection at $z = \frac{1}{2}$. It is clear that the flow field contains 30 convection rolls (15 pairs of counter-rotating rolls) where the width of a single convection roll is unity.

Figure 4 shows the spatial variation of the fluid velocity in a region containing several counter-rotating convection rolls. Figure 4 is an $x$-$z$ projection at $y = \Gamma_y/2$ showing a closeup view of the flow field shown in Fig. 3(a). The arrows are fluid
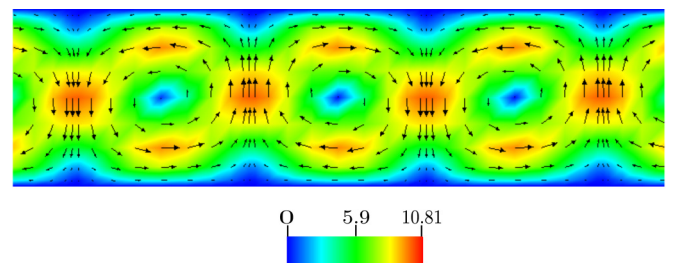


FIG. 4. A closeup view of the fluid velocity composing the counter-rotating convection rolls from Fig. 3. An $x$-$z$ projection is shown at $y = \Gamma_y/2$. The arrows are fluid velocity vectors and the color contours are of the fluid velocity magnitude where red is large and blue is small.
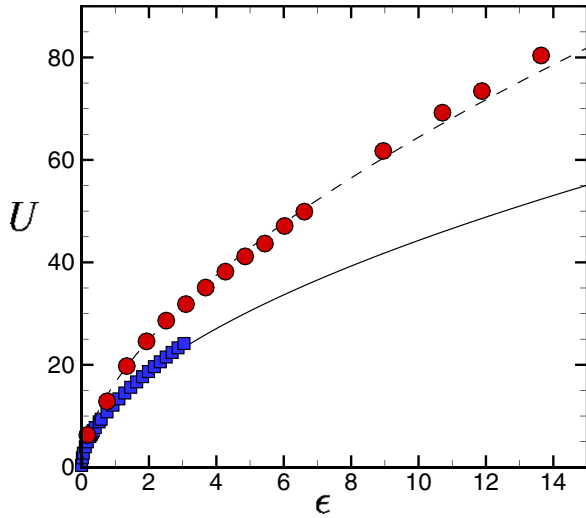
FIG. 5. The variation of the characteristic fluid velocity $U$ with the reduced Rayleigh number $\epsilon$. The squares (blue) are for a flow field of straight-parallel convection rolls in a rectangular domain and the circles (red) are for chaotic and weakly turbulent flow fields in a large cylindrical convection domain. The lines are power-law curve fits through the data where $U = 12.85\epsilon^{0.54}$ (solid line) and $U = 16.61\epsilon^{0.59}$ (dashed line).



FIG. 6. A propagating front in a field of straight-parallel convection rolls for Ra = 3000 and Le = 1. The color contours are of the concentration at the midplane $c(x, y, z = 1/2, t)$ where red is pure products ($c = 1$) and blue is pure reactants ($c = 0$). The region in-between indicates the location of the reaction zone which is traveling from left to right. The black lines are contours of the temperature field at $T = \frac{1}{2}$ which indicate the center line of the convection rolls. Three instances of time are shown (a) $t = 1$, (b) $t = 2$, and (c) $t = 3$ where $t$ is measured as the time since the initiation of the front at the left wall. (Additional parameters: $U = \text{Pe} = 10.81$, Da = 0.83.)

velocity vectors $\vec{u}$ and the color contours are of the magnitude of the fluid velocity where red represents large values and blue represents small values.

The characteristic velocity of the fluid $U$ plays an important role when describing the effect of the fluid motion on the propagating front. We use the time average of the maximum value of the fluid velocity magnitude at the horizontal midplane (away from the hot sidewalls) as the characteristic velocity $U$ of the flow field. For the flow field shown in Figs. 3 and 4, this yields $U = 10.81$.

Using our nondimensionalization, we have $\text{Re} = U/\text{Pr}$ where Re is the Reynolds number of the fluid flow. In all of our computations we have used $\text{Pr} = 1$ which yields $\text{Re} = U$. Our numerical results therefore explore the range of Reynolds numbers $0 \leqslant \text{Re} \lesssim 100$.

The variation of $U$ with the reduced Rayleigh number $\epsilon$ is shown in Fig. 5 where $\epsilon = (\text{Ra} - \text{Ra}_c)/\text{Ra}_c$. Each square symbol (blue) is from a numerical simulation in the box domain shown in Fig. 1 where we have also been careful to keep the number of convection rolls constant at 30 for all values of $\epsilon$. The box domain with hot sidewalls is stabilizing for convection rolls lined up in the $x$ direction which makes this possible.

For larger values of $\epsilon$ where $\epsilon \gtrsim 3$ the straight-parallel convection rolls eventually become unstable through a skew-varicose instability if we allow the simulation to continue for a long time. However, for our purposes we only require the straight and parallel convection rolls to persist for the duration of the front propagation that we study which is $t \lesssim 10$. For all of our simulations of fronts propagating in straight-parallel convection rolls this requirement is met. Figure 5 also includes data from numerical simulations for chaotic and weakly turbulent flows represented as circles (red) which will be discussed in more detail in Sec. III A 3.
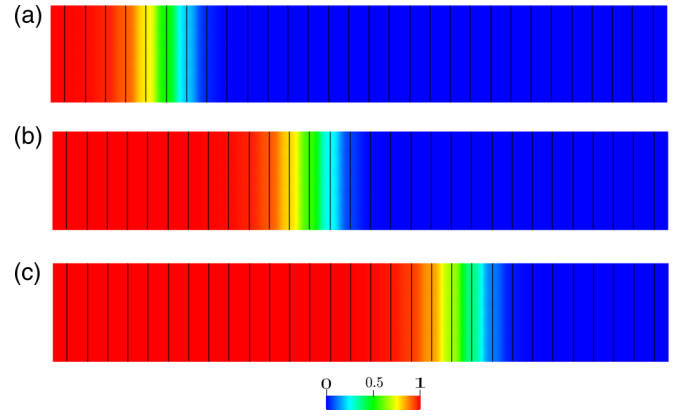
The solid black line in Fig. 5 is a power-law curve fit through the data of the form $U = 12.85\epsilon^{0.54}$. This is in agreement with the dependence $U \propto \epsilon^{1/2}$ which is expected near the convective threshold $\epsilon \ll 1$ [28]. However, it is interesting that this scaling behavior persists in our computations for $\epsilon$ much larger than this.

After establishing the straight and parallel convection rolls, a propagating front is initiated that travels from left to right through the convection rolls. Images showing the propagating front are given in Fig. 6 for the case of Le = 1. The concentration field is plotted as color contours at the horizontal midplane $c(x, y, z = 1/2, t)$ at three different times where $t$ is measured from the initiation of the front at the left wall. The front is propagating from left to right where red is pure products, blue is pure reactants, and the reaction zone is located in-between. The black lines indicate the center lines of the underlying convection rolls for reference.

It is clear that the thickness of the reaction zone is finite and that it is larger than the roll width for these conditions. This is expected since the reaction zone thickness in the absence of the flow for these conditions is predicted by Eq. (6) to be $\delta_0 = 2.67$. The reaction zone shows a smooth transition from red to blue across the front. This is expected due to the significant amount of diffusion that occurs for this case.

The propagating front for Le = 0.1 is shown in Fig. 7. In this case, the thickness of the reaction zone is smaller as expected for a smaller value of Le as given by Eq. (6). In addition, it is clear that the underlying fluid motion of the convection rolls now has more of an impact upon the reaction zone as illustrated by the nonsmooth transition from the red to blue across the front. This indicates the presence of more complicated structure of the reaction zone in the vertical $z$ direction.

The vertical structure of the reaction zones in Figs. 6 and 7 is shown in Fig. 8. A closeup view of the region near the
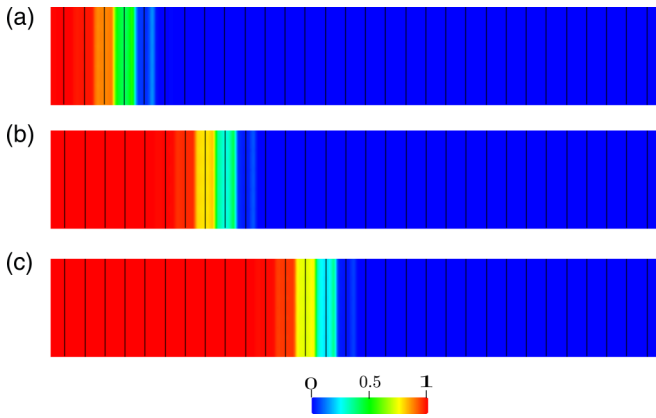
FIG. 7. A propagating front in straight-parallel convection rolls for Ra = 3000 and Le = 0.1 using the same conventions as Fig. 6 where (a) $t = 1$, (b) $t = 2$, and (c) $t = 3$. These images show that for this smaller value of the Lewis number the front and its dependence upon the flow field is more complex. (Additional parameters: $U = 10.81$, Pe = 100.81, Da = 0.83.)



FIG. 9. A closeup view of propagating fronts traveling left to right in a cellular flow field of convection rolls (Ra = 3000). The arrows represent the fluid velocity vector field and the horizontal extent of each panel is chosen to roughly include a single pair of counter-rotating convection rolls. The propagating front is the solid line which represents the $c = \frac{1}{2}$ level set. (a)–(d) Le = 1, and (e)–(h) Le = 0.1. The time between successive panels is 0.1 time units.

front is shown using a $x$-$z$ projection of the concentration field $c(x, y = \Gamma_y/2, z, t)$. The arrows represent the fluid velocity vectors of the underlying convection rolls. Figure 8(a) shows the front for Le = 1 and Fig. 8(b) shows the front for Le = 0.1. The influence of the convection rolls is evident in both images. However, the influence is strongest in Fig. 8(b) as indicated by the spiraling of the reaction into the core region of the convection rolls.

These interesting features of the geometry of the propagating front can be visualized by plotting the level-set contour of $c = \frac{1}{2}$ as shown in Fig. 9. Figures 9(a)–9(d) show a front traveling left to right through straight and parallel convection rolls for Ra = 3000 and Le = 1. Each panel is a closeup view of a region of the flow field containing a pair of counter-rotating convection rolls in the center. The arrows represent the vectors of the fluid velocity. The propagating front is shown as the solid line which is a contour of $c = \frac{1}{2}$ at a particular instant of time. The bending and distortion of the front is clearly visible due to the underlying convective flow field. Figures 9(e)–9(h) illustrate a propagating front for Ra = 3000 and Le = 0.1. In
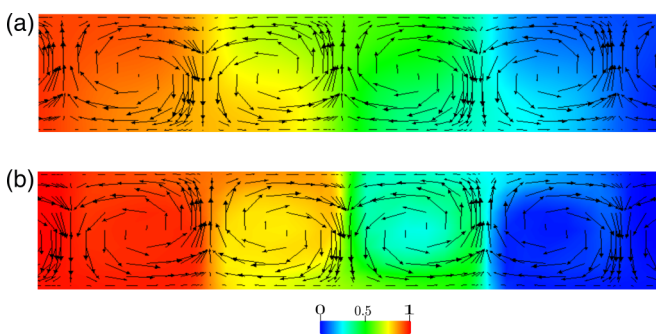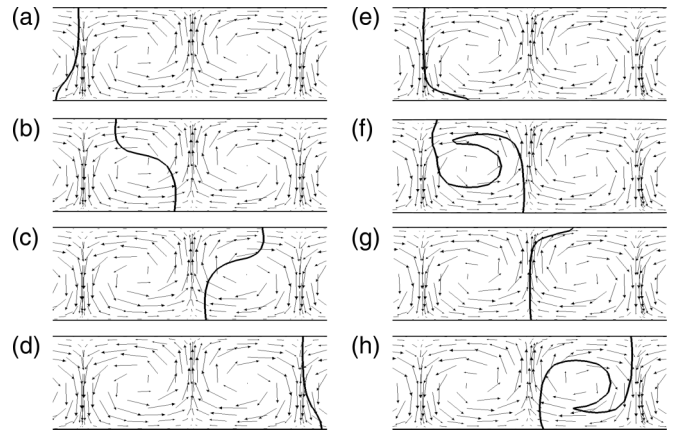
this case, the flow field has a much stronger effect upon the front geometry resulting in the cusp and spiral structures that are shown.

Once we have identified the location of the front, as shown in Fig. 9, it is straightforward to compute a front velocity as the time derivative of the front position. In order to account for the $z$ variation of the front we first compute the front velocity at a position $z$ and then compute the spatial average over all $z$ to yield a single number for the front velocity $v_f(t)$. Such an approach is well suited for the front shown in Figs. 9(a)–9(d). The front velocity computed in this way for this case is shown in Fig. 10 as the blue square symbols.

For the front shown in Figs. 9(e)–9(h) there are instances of time where there are multiple locations of the front at a single position $z$. In particular, this is clearly the case in Figs. 9(f) and 9(h). In this case, we track the average position of the front at a particular value of $z$. We then use these front positions to compute the front velocity as a function of $z$ at a particular time. Finally, the front velocity at time $t$ is computed by averaging these values over the $z$ direction. The time variation of the front velocity $v_f(t)$ computed in this way for the front shown in Figs. 9(e)–9(h) is shown in Fig. 10 using the blue diamond symbols.

We are interested in using the bulk burning rate approach to compute the front velocity for very complex fronts where it would be difficult to proceed by tracking the time variation of the intricate front position which is expected to be multivalued and disconnected in space. We next demonstrate that the bulk burning rate approach accurately captures the front velocity for this case where it is also straightforward to track the front position.

We use the bulk burning rate idea [see Eq. (7)] to compute the velocity of the propagating fronts shown in Figs. 6–9. Despite the vertical structure of the fronts shown in Figs. 8 and 9, we find that it is not necessary to compute the integral over the depth of the fluid layer when computing $v_f(t)$.
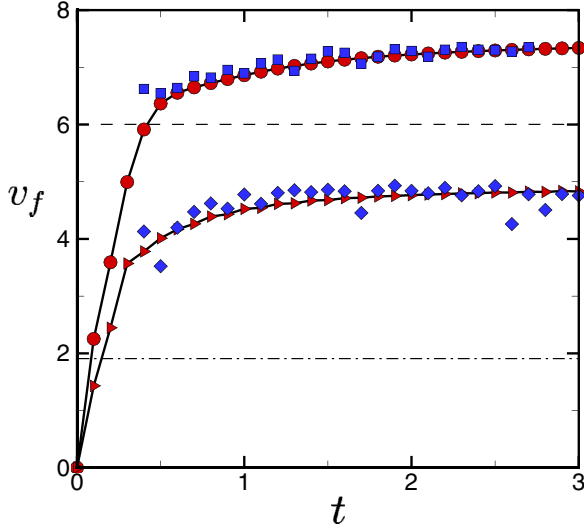


FIG. 8. A closeup view of the $x$-$z$ projection of the propagating fronts in Figs. 6 and 7. Color contours of $c(x, y = \Gamma_y/2, z, t)$ are shown of the region near the reaction zone where red is pure products $c = 1$ and blue is pure reactants $c = 0$. The black arrows are the fluid velocity vectors which indicate the counter-rotating convection rolls. (a) Le = 1, (b) Le = 0.1.

FIG. 10. The time variation of the front velocity $v_f(t)$ in the field of straight-parallel convection rolls at Ra = 3000 shown in Fig. 3. The blue symbols are $v_f(t)$ computed using the spatially averaged velocity of the level-set contours for $c = \frac{1}{2}$ shown in Fig. 9 with squares (Le = 1) and diamonds (Le = 0.1). The solid lines and red symbols are $v_f(t)$ computed using the bulk-burning-rate approach with circles (Le = 1) and triangles (Le = 0.1). The dashed and dashed-dotted lines indicate the front velocity in the absence of a flow field where $v_0 = 6.0$ (Le = 1) and $v_0 = 1.9$ (Le = 0.1), respectively. For these results $\bar{v}_f = 7.57$ (Le = 1) and $\bar{v}_f = 4.96$ (Le = 0.1).

Rather, the value of the front velocity computed using only data from the horizontal midplane slice at $z = \frac{1}{2}$ is sufficient. In particular, we will compute the front velocity using

$$v_f(t) = \int_0^{\Gamma_x} \frac{\partial c}{\partial t}\bigg|_{z=1/2} dx. \qquad (9)$$

For the fronts shown in Figs. 6 and 7, the error in using Eq. (9) is less than 0.2% when compared with the full calculation that includes the integral over the depth.

Overall, for more complicated fronts we find that the error can be slightly larger reaching values of several percent when determining $v_f(t)$. However, using Eq. (9) drastically reduces the amount of data needed to compute the front velocity and we will use this approach in all of our computations.

The time variation of $v_f(t)$ computed using Eq. (9) is shown in Fig. 10 using the red symbols where the circles are for Le = 1 and the triangles are for Le = 0.1. The dashed and dashed-dotted lines indicate the front velocity in the absence of fluid flow $v_0$. Overall, the agreement between the front velocity computations using the tracked fronts and using the bulk burning rate idea at the midplane is very good. In the remainder of our calculations we will use the bulk burning rate approach to compute the front velocity.

Figure 10 illustrates that the front velocity $v_f(t)$ increases rapidly at small times $t \lesssim 1$ and then slowly approaches an asymptotic value. Using Eq. (8) for $t \geqslant 1$ we obtain values for the asymptotic front speeds $\bar{v}_f$. These results clearly indicate enhancement to the front velocity due to the underlying flow field where $\bar{v}_f/v_0 = 1.26$ for Le = 1 and $\bar{v}_f/v_0 = 2.61$ for Le = 0.1. As expected, the enhancement is more significant
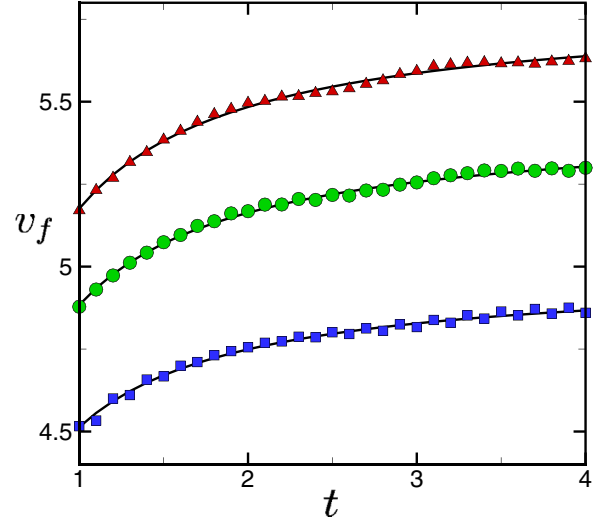


FIG. 11. Determination of the asymptotic front velocity $\bar{v}_f$ from $v_f(t)$ in a field of straight and parallel convection rolls. Results are shown for $v_f(t)$ where Le = 0.1 at three different values of the Rayleigh number Ra = (3000, 3600, 4200) using squares (blue), circles (green), and triangles (red), respectively. The symbols are values of $v_f(t)$ computed using Eq. (7). The solid lines are curve fits through the data using Eq. (8) which yield $\bar{v}_f = 4.98, 5.44,$ and 5.79. The velocity in the absence of fluid flow is $v_0 = 1.9$ from Eq. (5).

when the Lewis number is smaller where the role of molecular diffusion is less important.

Figure 11 shows the effectiveness of using Eq. (8) to determine $\bar{v}_f$ for several results of $v_f(t)$ for fronts traveling in straight-parallel rolls with Le = 0.1. Results are shown for the three different Rayleigh numbers Ra = (3000, 3600, 4200) as squares (blue), circles (green), and triangles (red). The solid lines are curve fits through the data using Eq. (8).

Using this approach, we computed the variation of the asymptotic front velocity $\bar{v}_f$ in a field of straight-parallel rolls for a large range of values of the characteristic velocity $U$. Results for Le = 1 are shown in Fig. 12. Each symbol is $\bar{v}_f$ computed from a separate simulation where each value of $U$ is the result of changing the Rayleigh number for the convective flow field.

The data of Fig. 12 are separated into two different groups. The circles (blue) are results where the Damköhler number Da > 1 and the squares (red) are where Da < 1. Since Le = 1 we also have $U = \text{Pe}$ for the results in this figure.

The circles (blue) represent the regime where Da > 1 and Pe $\lesssim$ 10 which can be described as a fast reaction and slow advection regime. The squares (red) represent Da < 1 and Pe $\gtrsim$ 10 which can be described as a slow reaction and fast advection regime. As a result, the variation of $\bar{v}_f$ in these two regimes is quite different and there is a clear transition as the value of $U$ is increased.

The line through the circles representing the slow advection regime is a curve fit of the form $\bar{v}_f/v_0 = 1 + 0.09(U/v_0)^2$. These results suggest the quadratic dependence $\bar{v}_f/v_0 \propto (U/v_0)^2$ that is in agreement with the Clavin-Williams relation [46]. This quadratic dependence can be recovered by expanding the concentration $c$ in the small
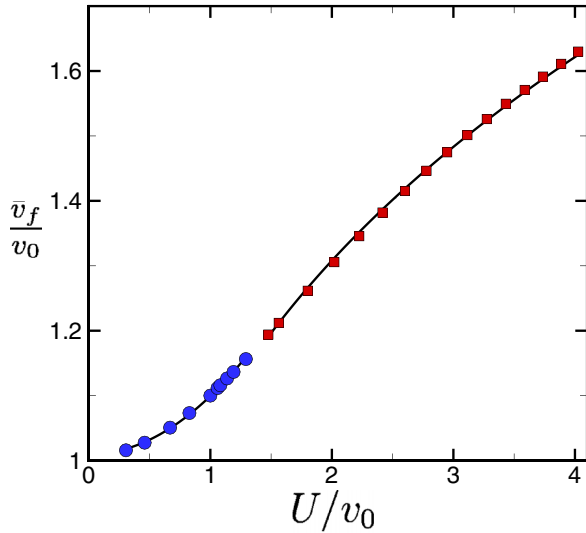
FIG. 12. The variation of $\bar{v}_f/v_0$ with $U/v_0$ for a front traveling through straight and parallel convection rolls with Le = 1. Each data symbol is the result from a distinct numerical simulation. The circles (blue) indicate Da > 1 and the squares (red) indicate Da < 1. The solid lines are curve fits through the data where $\bar{v}_f/v_0 = 1 + 0.09(U/v_0)^2$ for Da > 1 and $\bar{v}_f/v_0 = 1.06(U/v_0)^{0.31}$ for Da < 1. For these results $0.375 \leqslant$ Da $\leqslant 4.9$, $0 <$ Pe $\leqslant 25$, DaPe = 9, $v_0 = 6$, and Pe = $U$.

parameter $U$ and solving Eq. (4) using simple free slip boundary conditions and a cellular flow. The line through the squares representing the fast advection regime is a curve fit of the form $\bar{v}_f/v_0 = 1.06(U/v_0)^{0.31}$.

Figure 13 shows the variation of $\bar{v}_f/v_0$ with $U/v_0$ for the case where Le = 0.1 and the fluid motion is expected to have a
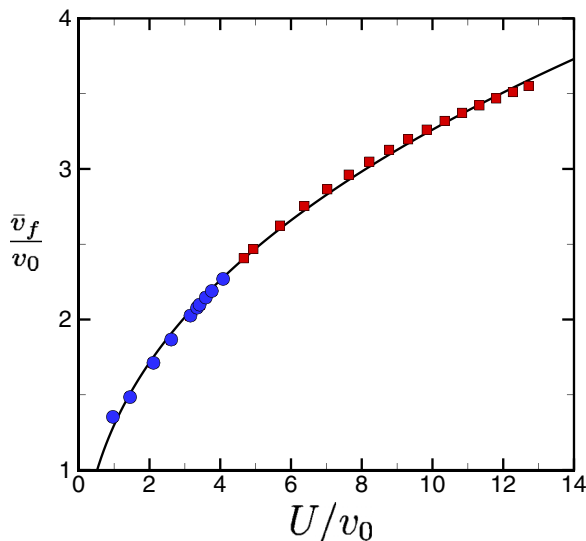


FIG. 13. The variation of $\bar{v}_f/v_0$ with $U/v_0$ for a front traveling through straight and parallel convection rolls with Le = 0.1. Circles (blue) indicate Da > 1, squares (red) indicate Da < 1, and the solid line is a curve fit through the squares using $\bar{v}_f/v_0 = 1.30(U/v_0)^{0.40}$. For these results $0.375 \leqslant$ Da $\leqslant 4.9$, $0 <$ Pe $\leqslant 250$, DaPe = 90, and $v_0 = 1.9$.

larger impact upon the propagating front. For these results, the Damköhler numbers remain the same as in Fig. 12, however, the Péclet numbers are now an order of magnitude larger since Pe = 10$U$. The results of Fig. 13 are also collected into the two groups indicated by the circles (blue) where Da > 1 and the squares (red) where Da < 1. The solid line is a curve fit through the square symbols and is of the form $\bar{v}_f/v_0 = 1.30(U/v_0)^{0.40}$. For this case it is numerically difficult to probe the regime where $U/v_0 < 1$ and, as a result, we do not have values yielding a quadratic dependence here.

For fronts traveling through an idealized cellular flow in the limit where Pe $\gg$ 1 and DaPe $\gg$ 1, which represents propagating fronts where the flow velocity is important and the diffusion timescale is the largest, theoretical predictions yield scaling behavior of the form $\bar{v}_f \propto U^{\alpha_f}$ [26,27].

In the slow reaction limit where Da $\ll$ 1, the predicted scaling exponent is $\alpha_f = \frac{1}{4}$ [26,27,47–50]. The physical insight behind this result is that the front propagation can be described as enhanced diffusion with a diffusion coefficient that varies as the square root of the flow velocity. From rather general arguments it can be shown that $\bar{v}_f$ has an upper bound that varies as the square root of this effective diffusion coefficient which then yields the exponent $\alpha_f = \frac{1}{4}$.

In the fast reaction regime where Da $\gg$ 1, the scaling exponent is $\alpha_f = \frac{3}{4}$ [26,27]. In this case, the effective diffusion argument remains valid, however, there is a renormalization of the timescales. The reaction zone thickness is now small compared to the length scale describing the cellular flow $\delta \ll L$. As a result, the reaction zone fills each vortex while spiraling inward on the advective timescale $\tau_U$. The enhanced transport resulting from this convective timescale leads to the exponent $\alpha_f = \frac{3}{4}$.

Although our results are not for the same conditions as that of Refs. [26,27], it is insightful to compare with these predictions. An important difference is that the flow field of Refs. [26,27] is an idealized cellular flow where the sinusoidal fluid velocity reaches a maximum at the bottom and top surfaces. For Rayleigh-Bénard convection, this would more closely correspond to free slip boundary conditions at the bottom and top boundaries. In our simulations we have used no-slip boundary conditions where the fluid velocity at all walls is zero. It is interesting to point out that recent experiments studying propagating fronts in cellular electroconvective flows probed the role vortex structure by using rigid and free boundaries and found that the fronts were faster for free boundary conditions [21]. In addition, the nondimensional parameters of our simulations span a range of values that include regions where the approximations of the theoretical predictions become questionable.

A good portion of our results fall into the regime that could be expected to be described by theoretical predictions for the slow reaction limit where Da $\ll$ 1 which yields $\alpha_f = \frac{1}{4}$. This limiting situation is most relevant to the squares of Figs. 12 and 13 where we find scaling exponents of $\alpha_f = 0.31$ (Le = 1) and $\alpha_f = 0.40$ (Le = 0.1), respectively.

In our study, when we decrease Le for a particular flow field, the result is the increased importance of advection as captured by the increase in Pe. In light of this, it is reasonable to expect our scaling exponents to increase with decreasing Lewis numbers. However, it is interesting to point out that our
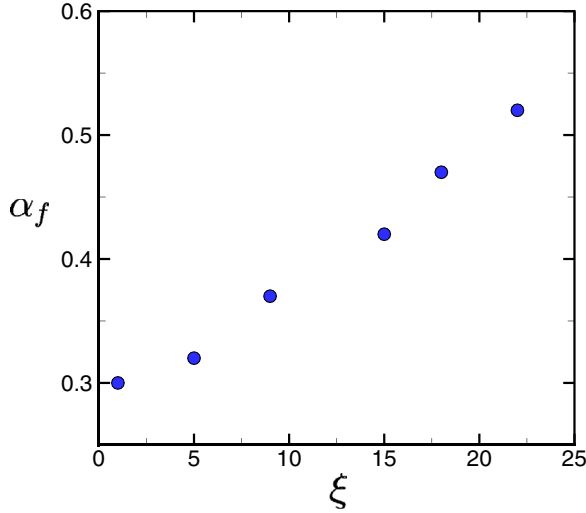
FIG. 14. The variation of the scaling exponent $\alpha_f$ of the front velocity with the reaction rate $\xi$ for fronts traveling though straight-parallel convection rolls at Le = 0.1. $\alpha_f$ at a particular value of $\xi$ was determined by conducting seven numerical simulations for different values of $U$ and then fitting the results with $\bar{v}_f \propto U^{\alpha_f}$.

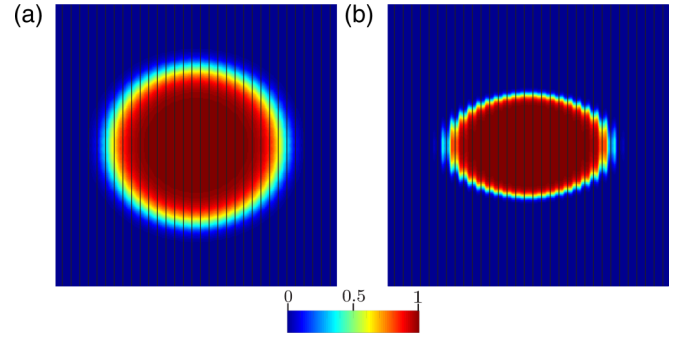

FIG. 15. Propagating fronts in a spatially extended field of straight and parallel convection rolls for Ra = 2400, $\Gamma = 30$ with (a) Le = 1, $t = 1.5$ and (b) Le = 0.1, $t = 2.0$ where $t$ is measured from the initiation of the front. The front is initiated at the center of the domain and is propagating outward. The color contours are of the concentration field $c$ where red is pure products and blue is pure reactants. The solid black lines indicate the pattern of the convection rolls. The front is slightly elliptical for Le = 1 as indicated by the weak dependence of the front on the local convection roll orientation. For Le = 0.1 the effect of the convection roll orientation is significant and results in an elliptical front with higher eccentricity.

scaling exponents are slightly larger than the predicted values for the idealized flow field. This may be due, in part, to the variation of the vortex structure of the cellular flow for the different boundary conditions as explored in Ref. [21].

Our results do not capture the fast reaction limit that requires Da ≫ 1 while also satisfying Pe ≫ 1. The circles of Figs. 12 and 13 quantify the range $1 \lesssim$ Da $\lesssim 26$. In Fig. 12, where Pe $\lesssim 10$ and $U/v_0 \lesssim 1.5$, we find a very rapid increase in the front velocity with an increase in the flow velocity that yields an exponent of $\alpha_f = 2$ for the case Le = 1. However, in Fig. 13 where Pe $\lesssim 100$ and $U/v_0 \lesssim 5$, we find that the scaling yields $\alpha_f \approx 0.4$ for Le = 0.1.

We probe these ideas further by exploring the variation of the scaling exponent $\alpha_f$ with the reaction rate $\xi$ at a fixed value of Le. In Fig. 14 we show results for a flow field of straight-parallel rolls with Le = 0.1 where we investigate the range of reaction rates $1 \leqslant \xi \leqslant 22$. For each value of $\xi$ we performed seven numerical simulations to quantify the front velocity $\bar{v}_f$ through convection rolls for a range of $U$ by using the Rayleigh numbers $3900 \leqslant$ Ra $\leqslant 5700$. From these simulations we determined the scaling exponent by fitting the results to $\bar{v}_f \propto U^{\alpha_f}$ for that particular value of $\xi$. Figure 14 shows results obtained in this manner for six different values of $\xi$.

Figure 14 clearly indicates that the scaling exponent $\alpha_f$ increases with increasing reaction rate $\xi$. For all of the results in this figure $145 \lesssim$ Pe $\lesssim 205$ which is in the large Péclet number regime. However, the Damköhler number varies significantly where it takes on its smallest values of Da $\approx 0.05$ for $\xi = 1$ and its largest values of Da $\approx 1$ for $\xi = 22$. It is interesting that our value of $\alpha_f \approx 0.3$ for $\xi = 1$ is similar to the prediction [26,27] that $\alpha_f = \frac{1}{4}$ for Da $\ll 1$ and DaPe $\gg 1$ despite the fact that our results do not satisfy this latter constraint where we have DaPe = 10.

For our results, the largest reaction rate we have explored is $\xi = 22$ where Pe > 100 and Da $\approx 1$. We are not aware of

a theoretical prediction for this regime. However, we would expect the increasing trend of $\alpha_f$ with $\xi$ to approach $\alpha_f \approx \frac{3}{4}$ for $\xi \gg 1$ in agreement with the theoretically predicted value for Da $\gg 1$ and DaPe $\gg 1$ [26,27]. The large $\xi$ regime is difficult to explore numerically using our approach for several reasons. One difficulty is the increased front velocity as indicated by Eq. (5) and another is that the reaction zone becomes very sharp as indicated by Eq. (6). We have not explored this regime further.

### 2. Orientation of straight-parallel rolls

Our discussion up to this point has quantified the velocity of a propagating front in a field of straight and parallel convection rolls where the front is propagating in the direction perpendicular to the axis of the convection rolls. In this case, this direction is parallel to the wave vector $\vec{q}$ of the convection rolls. However, in a more complex flow field the propagating front will encounter rolls at arbitrary angles relative to the front.

As a measure to quantify the front speed as a function of its direction of propagation relative to the orientation of the convection rolls, we will use the reaction zone angle $\phi$. We define the reaction zone angle $\phi$ as the angle between the local wave vector $\vec{q}$ of the convection rolls and the radial direction in the region of the reaction zone. In all of our computations we will be interested in quantifying the velocity of the propagating front in the radial direction. As a result, it will be useful to describe the front using the polar coordinates $(r, \theta)$ where the origin is at the center of the domain and $0 \leqslant \theta \leqslant 2\pi$.

In order to compute the radial velocity of the propagating front $v_r$ for all reaction zone angles $\phi$ from a single numerical simulation, we use the configuration shown in Fig. 15. We use a large square convection domain containing a field of straight-parallel convection rolls. The aspect ratio of this
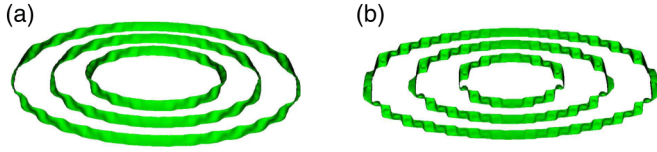
(a)                                          (b)



FIG. 16. The spatial structure of the propagating fronts shown in Fig. 15 where (a) Le = 1 and (b) Le = 0.1. In each panel, the front is shown at three different times where the front is represented as the level-set surface where $c = \frac{1}{2}$ where the front is propagating from the center of the domain outward. The image is tilted at a small angle in order to improve visualization of the front. (a) $t = 1.0, 1.5, 2.0$, (b) $t = 1.0, 2.0, 3.0$.

domain is $\Gamma = L_s/d = 30$ where $L_s$ is the side length of the square domain. Again, we use hot sidewalls at the left ($x = 0$) and right ($x = \Gamma$) edges of the domain to create the time-independent pattern of $x$ rolls. The center line of the convection rolls are indicated by the black solid lines.

There is a limited range of Rayleigh numbers $Ra_c \leqslant Ra \lesssim 2400$ where such a large field of parallel rolls remain stable. This restricts the values of $U$ that can be explored using this approach. However, it is insightful to quantify the variation of $v_r$ with respect to $\phi$ for the convection patterns we have been discussing where possible. Furthermore, these insights for fronts propagating through straight and parallel convection rolls will be useful when we discuss propagating fronts in chaotic flow fields.

After establishing the pattern of convection rolls, we initiate the propagating front at the center of the domain with an initial condition of the form

$$c(r, \theta, z, t_0) = e^{-r^2}, \qquad (10)$$

where $t_0$ is the time at which the initial condition is applied. This initial condition is steep enough to generate a pulled front [1]. The front then propagates outward radially towards the sidewalls of the domain. In Fig. 15 the color contours are of the concentration field where red is products, blue is reactants, and the reaction zone is indicated by the color variation inbetween where the time shown is after its initiation $t > t_0$.

Figure 16 illustrates the geometry of the propagating fronts at three different times for the same conditions as Fig. 15. The front is visualized as the level-set contour of the concentration field where $c = \frac{1}{2}$ and is shown by the green ribbonlike structures. The fronts are traveling from the center of the domain outward. The fronts shown in Fig. 16 clearly reflect the influence of the underlying convection rolls. The front geometry is more complex in Fig. 16(b) as expected since these results are for a smaller Lewis number.

We compute $v_r(\theta, t)$ using the bulk burning rate idea which we now apply to the radially propagating front where

$$v_r(\theta, t) = \int_0^\Gamma \frac{\partial}{\partial t} c(r, \theta, z = 1/2, t) dr. \qquad (11)$$

Due to the symmetry of the problem, each quadrant of the square convection domains shown in Fig. 15 contains a propagating front over the range of the reaction zone angle of $0 \leqslant \phi \leqslant \pi/2$.
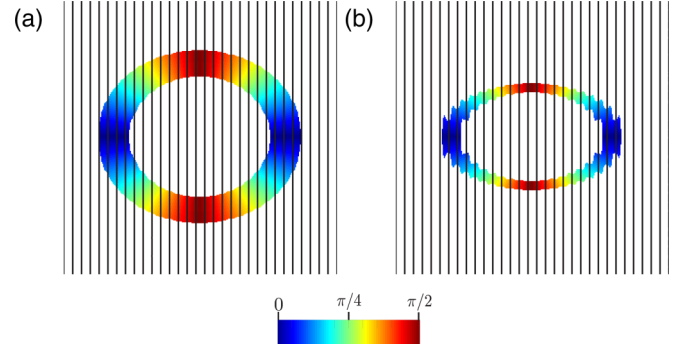
(a)                                          (b)



FIG. 17. The spatial variation of the reaction zone angle $\phi$ for the fronts traveling through the convection rolls shown in Fig. 15. $\phi$ is computed where the concentration is in the range $0.1 \leqslant c \leqslant 0.9$. The black lines indicate the location of the convection rolls. (a) Le = 1 and (b) Le = 0.1.

The spatial variation of the reaction zone angle is shown explicitly in Fig. 17 using color contours. Regions where the direction of front propagation is perpendicular to the axis of the convection rolls are blue ($\phi = 0$) and regions where the front is traveling parallel to the roll axis are red ($\phi = \pi/2$). The reaction zone angle is shown for any location in space where the concentration is within the range $0.1 \leqslant c \leqslant 0.9$. This threshold is not meant to capture the geometry of the front interface, but rather to include the spatial region that contributes significantly to the front velocity computation using Eq. (11). In addition, this threshold is also chosen to align with Eq. (6) which describes the thickness of the reaction zone in the absence of fluid motion. We will use the front geometry captured by the $c = \frac{1}{2}$ level set (for example, see Fig. 16) in Sec. III B when we quantitatively explore the geometry of the front. Using results of the type shown in Fig. 17, we will represent the front velocity as $v_r(\langle\phi\rangle, t)$ where $\langle\phi\rangle$ is the radially averaged value of the reaction zone angle $\phi$ at a particular value of the polar angle $\theta$.

Figure 18 shows the variation of the front velocity with the radially averaged reaction zone angle $\langle\phi\rangle$ for the fronts shown in Fig. 15. For a reaction zone angle of $\langle\phi\rangle = \pi/2$, there is no fluid velocity in the direction of the propagating front. As a result, the front velocity will asymptotically approach the bare
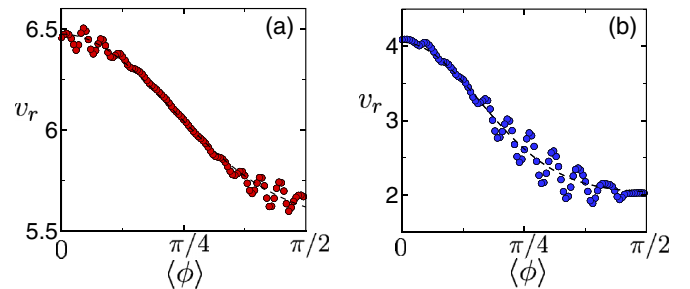


FIG. 18. The variation of the instantaneous radial front velocity $v_r$ with the radially averaged reaction zone angle $\langle\phi\rangle$ for the fronts shown in Fig. 15 where (a) Le = 1 and (b) Le = 0.1. The dashed lines are Gaussian curve fits of the form (a) $v_r = 5.54 + 0.93e^{-\langle\phi\rangle^2}$ and (b) $v_r = 2.03(1 + e^{-2\langle\phi\rangle^2})$.
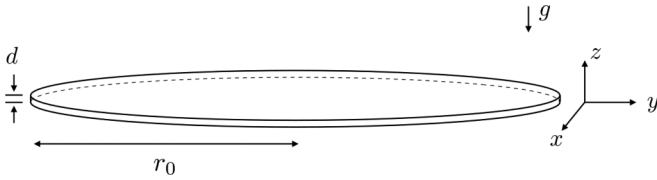
FIG. 19. The cylindrical domain used for our simulations of chaotic and weakly turbulent convection. The radius of the domain is $r_0$, the depth of the fluid layer is $d$, the directions of the Cartesian coordinates $(x, y, z)$ are shown, and $g$ is the acceleration due to gravity. The bottom wall is held at a constant hot temperature, the top wall is held at a constant cold temperature, and the lateral sidewalls are perfect thermal conductors. The aspect ratio of the domain is $\Gamma = r_0/d = 40$ (figure is drawn to scale).

front velocity in this direction such that $\bar{v}_r(\langle \phi \rangle = \pi/2) = v_0$ as expected. The case of $\langle \phi \rangle = 0$ is what is shown in Figs. 6–13 where $v_r(\langle \phi \rangle = 0, t)$ is the largest front velocity and the underlying fluid velocity has the largest effect.

Figure 18(a) shows results for Le = 1 where molecular diffusion is significant relative to advection. For this case, the flow field weakly affects the front velocity and, as a result, the increase in the radial front velocity for decreasing reaction zone angle is small. Figure 18(b) shows the variation of the instantaneous front velocity with the reaction zone angle for Le = 0.1 where advection is now significant. In this case, the front velocity increases by a factor of 2 when going from $\langle \phi \rangle = \pi/2$ to 0. The oscillations in the data with $\langle \phi \rangle$ are related to the wavelength of the underlying convection rolls. These oscillations are more significant for Le = 0.1 where the impact of advection is more significant. The dashed lines in these figures are Gaussian curve fits through the data which capture the overall trend. We currently do not have a theoretical justification for this particular functional form.

### 3. Fronts in chaotic flow fields

We next explore the propagation of fronts in the presence of chaotic and weakly turbulent flow fields. In this case, we use a large cylindrical convection domain with an aspect ratio of $\Gamma = r_0/d = 40$ where $r_0$ is the radius of the cylindrical domain. A schematic of the cylindrical convection domain is shown in Fig. 19

A typical chaotic flow field is shown in Fig. 20 for the case of Ra = 9000. Figure 20 shows four different representations of the same flow field using color contours of different variables at the horizontal midplane $z = \frac{1}{2}$. For all of the panels of Fig. 20 we have set the minimum and maximum values of the color bars to reflect the minimum and maximum values of the variable that is plotted.

Figure 20(a) shows the typical convention of representing the convective flow field using color contours of the temperature field where red is hot rising fluid and blue is cold falling fluid. In this representation, the complex pattern of convection rolls is visible. Figure 20(b) shows color contours of the vertical component of the velocity field $w$ where red is a large positive value indicating upward fluid motion and blue is a large negative value indicating downward fluid motion. It is clear by comparing Figs. 20(a) and 20(b) that the temperature field $T$ and the vertical velocity field $w$ are very similar as
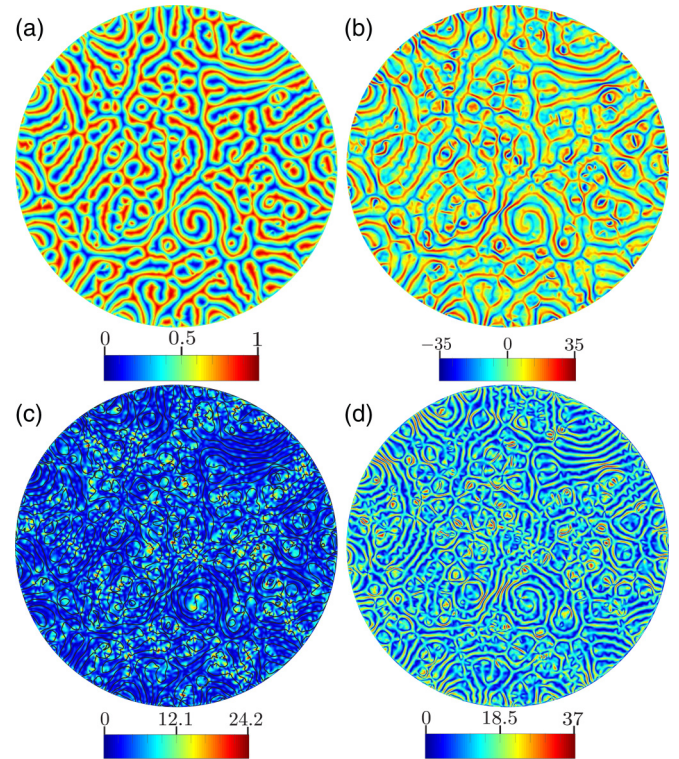


FIG. 20. Several representations of a flow field of chaotic convection in a large cylindrical domain with $\Gamma = 40$ for Ra = 9000 using color contours at the horizontal midplane $z = \frac{1}{2}$. (a) Contours of the temperature field where red is hot rising fluid and blue is cold falling fluid. (b) Contours of the fluid velocity $w$ in the $z$ direction where red is an upward velocity representing rising fluid and blue is a downward velocity representing falling fluid. (c) The magnitude of the fluid velocity in the $x$-$y$ plane $|\vec{u}_\perp|$ where red is a large magnitude and blue is a small magnitude. (d) The magnitude of the fluid velocity $|\vec{u}|$ where red is large and blue is small.

expected. The vertical component of the velocity is the largest component of the velocity for these convective flows.

Figure 20(c) shows color contours of the magnitude of the fluid velocity in the $x$-$y$ plane $|\vec{u}_\perp|$ where $\vec{u}_\perp = (u, v)$. Red is a large magnitude, blue is a small magnitude, and the black contours represent the center line of the underlying convection rolls for reference. It is no longer possible to discern the convection roll pattern from the color contours of $|\vec{u}_\perp|$. The magnitude of the velocity in the $x$-$y$ plane is very complicated and disordered with localized regions of large magnitude. The localized regions of large magnitude are often located near defect structures in the flow field patterns, but this is not always the case. Although the magnitude of $|\vec{u}_\perp|$ is smaller than that of $|w|$ shown in Fig. 20(b) it is clear that the in-plane velocity is significant. The localized regions of large magnitude of $|\vec{u}_\perp|$ are dynamic and change with the pattern dynamics.

Lastly, in Fig. 20(d) the magnitude of $|\vec{u}|$ is shown using color contours. Overall, using this representation it is possible to determine the convection roll pattern while also identifying localized regions of large fluid velocity. It is clear that regions of large velocity occur both near defect structures and also in regions of straight-parallel convection rolls. Figure 20
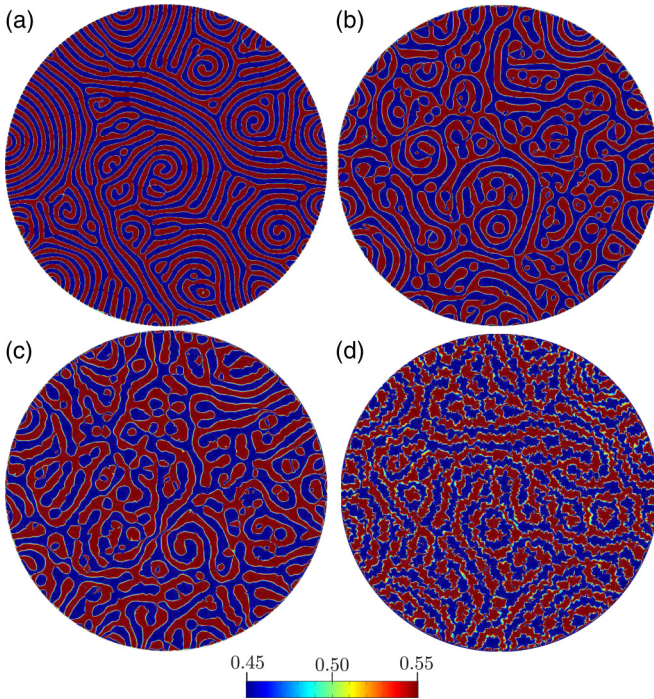
FIG. 21. Chaotic and weakly turbulent flow fields for convection in a large cylindrical domain where $\Gamma = 40$. Color contours are shown of the temperature field at the horizontal midplane $T(x, y, z = 1/2, t)$ at a specific time $t$. Red is hot rising fluid and blue is cold falling fluid. (a) Ra = 3000, (b) Ra = 6000, (c) Ra = 9000, and (d) Ra = 25 000.



FIG. 22. Propagating fronts in chaotic and weakly turbulent flow fields for Le = 1 where (a) Ra = 9000, (b) Ra = 13 000, and (c) Ra = 25 000. The solid black lines indicate the location of the convection rolls. Color contours of the concentration field are plotted at the horizontal midplane $c(x, y, z = 1/2, t)$ where red indicates $c = 1$ (pure products), blue indicates $c = 0$ (pure reactants), and the region in-between indicates the reaction zone. The fronts are shown at a time $t$ after the initiation of the front where (a) $t = 3$, (b) $t = 3$, and (c) $t = 2.5$.

illustrates the spatially disordered flow field of chaotic convection that we will use to explore front propagation.

Typical images of the flow fields are shown in Fig. 21 for the range of Rayleigh numbers $3000 \leqslant \text{Ra} \leqslant 25\,000$ using color contours of the temperature field at the horizontal midplane $T(x, y, z = \frac{1}{2})$ at a particular time $t$. These flow fields are primarily composed of convection rolls and the magnitude of the velocity field for any of these images can be determined from Fig. 5.

As the Rayleigh number is increased, the flow becomes more complex. For these conditions, it has been shown that the convective dynamics are chaotic which yields a spectrum of positive Lyapunov exponents [51,52]. For example, using the results of [51] the Kaplan-Yorke dimension [53] of the attractor describing the dynamics of the flow field shown in Fig. 21(b) can be estimated to be $D_\lambda \approx 400$. Furthermore, the convective dynamics we explore here is also expected to be in the extensively chaotic regime [51,52].

Although the flow fields of Fig. 21 are mostly composed of convection rolls, they are significantly more complicated than the flow fields we have explored so far. There is a now a complex spatial and temporal variation to the patterns. In addition, the patterns now contain many defect structures that nucleate and annihilate which play an integral role in the overall dynamics.

For Ra $\lesssim 10^4$ this is the spiral defect chaos state of Rayleigh-Bénard convection [54]. Furthermore, for Ra $\gtrsim 10^4$ [for example, see Fig.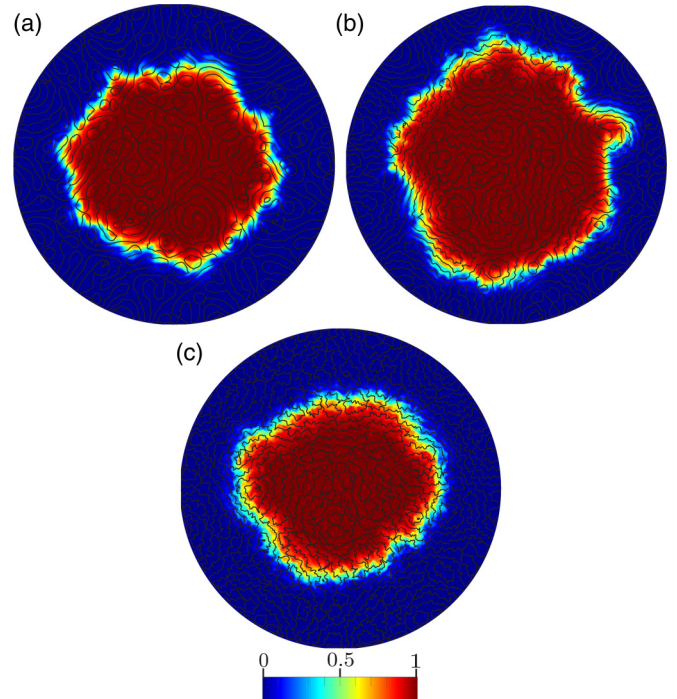 21(d)] the flow fields also exhibit an oscillatory instability which results in small-scale features that travel axially along the convection rolls [55].

Although all of our flow fields in the cylindrical convection domains are chaotic and have at least one positive Lyapunov exponent [52], we will sometimes refer to the chaotic flow fields that have also undergone the oscillatory instability as weakly turbulent flow fields. We use weakly turbulent to indicate that the spatial structure of the convection rolls has begun to deteriorate, which would continue toward the eventual generation of plume structures at much larger Rayleigh numbers. In the following, we quantify and explore how these additional complexities of the flow field affect a propagating front.

We first establish a flow field where all initial transients have decayed. This requires long-time numerical simulations of the Boussinesq equations on the order one horizontal diffusion time $\tau_h$ where $\tau_h = \Gamma^2$. We next initiate the reaction at the center of the domain using an initial condition of the form given by Eq. (10). This creates a pulled front propagating from the center of the domain toward the lateral sidewalls.

Images of propagating fronts for Ra = 9000, 13 000, and 25 000 are shown in Fig. 22 for Le = 1. The color contours are of the concentration field $c$ using our convention where red is products, blue is reactants, and the reaction zone is in-between. The solid black lines indicate the complex pattern of the underlying convection rolls.
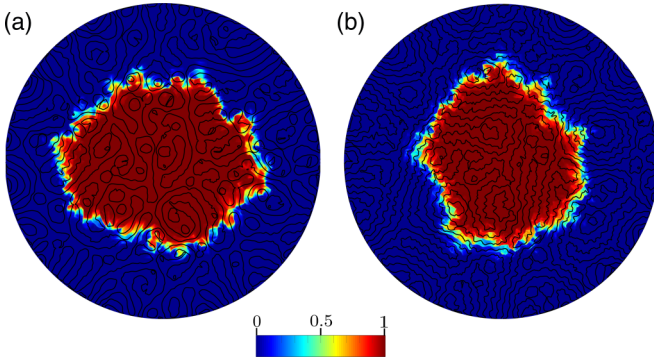
(a)                         (b)



0        0.5        1

FIG. 23. Propagating fronts in a chaotic flow for Le = 0.1 where (a) Ra = 9000 and $t = 4$ and (b) Ra = 13 000 and $t = 3$ using the same conventions as Fig. 22.

Figure 23 illustrates the front for Ra = 9000 and 13 000 for Le = 0.1. The front is now much more complicated due to the stronger influence of advection. Using our numerical approach, Ra = 13 000 was the largest value of the Rayleigh number we could explore for Le = 0.1. For small values of the Lewis number, the reaction zone features become very intricate and difficult to resolve which would require a more sophisticated numerical approach using specialized filters or particle tracking approaches which we have not pursued here [56,57].

Figure 24 illustrates the geometry of the propagating front for the conditions shown in Fig. 23(b). In Fig. 24 the propagating front is represented as the $c = \frac{1}{2}$ level-set contour. The three green ribbonlike structures show the propagating front at three different times as it travels from the center of the domain outward. The entire image has been rotated to make it possible to visualize the intricate nature of the propagating front surface. The front geometry is now quite complex and wrinkled due to the underlying chaotic flow field dynamics.

The characteristic velocity of the fluid $U$ for these chaotic flows is represented as the circles (red) in Fig. 5. Although the flow field is chaotic, the coefficient of variation of $U$ is less than 3% for the entire range of Rayleigh numbers we have explored here. It is interesting to point out that at the same value of Ra, the characteristic fluid velocity is larger for the chaotic flow fields than it is for the straight-parallel convection
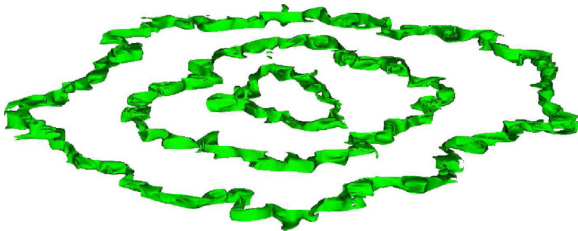


FIG. 24. The propagating front surface in a chaotic flow for Le = 0.1 and Ra = 13 000. The level set of the concentration field at $c(x, y, z, t) = \frac{1}{2}$ is shown in green at three different instances of time $t$ where $t = 1, 2, 3$. The front is propagating from the center outwards and the domain is shown at an angle to show the spatial features of the front. This particular front is also represented in Fig. 23(b).

rolls. The regions in the chaotic flow fields where the fluid velocity is large is connected in a complicated manner to the rapidly varying patterns of convection rolls. Regions of large fluid velocity occur both near the defect structures and within patches of parallel convection rolls.

For the propagating fronts in the chaotic flow fields, we compute the radial velocity of the front $v_r(\theta, t)$ using Eq. (11) evaluated at the horizontal midplane $z = \frac{1}{2}$ for a particular value of the polar coordinate $\theta$. The front velocity at any time $v_f(t)$ is the azimuthal average of $v_r(\theta, t)$ and the long-time asymptotic front velocity $\bar{v}_f$ is again found using Eq. (8).

We have found that using only the horizontal midplane to compute the front velocity results in an error of approximately 1% when compared to using the full three-dimensional front for this calculation. As a result of the significant reduction in the cost of the computation, all of our results for the front velocities are based upon the effective two-dimensional front traveling outward at the midplane as shown in Figs. 22 and 23.

Figure 25 illustrates the variation of the asymptotic front velocity over a wide range of conditions including chaotic flow fields and flow fields of time-independent straight-parallel convection rolls. Figure 25(a) shows the variation of $\bar{v}_f$ with the characteristic fluid velocity $U$ and (b) presents the same data scaled to show $\bar{v}_f/v_0$ versus Pe on a log-log scale.

The circles (red) and diamonds (green) are results for a front propagating in a chaotic flow field where Le = 1. The squares (blue) and triangles (green) are chaotic flow field results where Le = 0.1. Each filled data symbol is the average value of $\bar{v}_f$ from three separate numerical simulations performed at these parameters. The diamonds and triangles (green) indicate results where the flow field is above the threshold for the oscillatory instability ($U \gtrsim 40$ and Ra $\gtrsim 10^4$). The standard deviation of the results about their mean value are represented as error bars. For reference, the open circles and open squares represent the previously discussed asymptotic front speeds for fronts traveling through fields of straight-parallel convection rolls with a reaction zone angle of zero in the rectangular geometry of Fig. 1 for Le = 1 and Le = 0.1, respectively.

All of the lines through the data points in Fig. 25 are power-law curve fits of the form $\bar{v}_f \propto U^{\alpha_f}$. The scaling exponents $\alpha_f$ for several cases of particular interest are collected in Table I.

We first discuss the results for a front propagating in a chaotic flow field when Le = 1. We again find a power-law scaling for the variation of the front velocity with the underlying fluid velocity. The solid line through the circles in Fig. 25(a) is a curve fit of the form $\bar{v}_f = 3.77U^{0.27}$. There is a significant increase in the front velocity due to the oscillatory instability as indicated by the diamonds and these values are not included in this fit.

It is interesting to highlight that the fronts propagating in spiral defect chaos (filled circles) are always *slower* than the fronts traveling with a reaction zone angle of zero through a time-independent field of straight-parallel rolls with the same value of $U$ (open circles). The dashed-dotted line through the open circles is the power-law curve fit through the results for a front propagating in straight-parallel rolls where $\bar{v}_f \propto U^{0.31}$ (see Fig. 12). This suggests that one effect of the chaotic pattern of convection rolls is to lower the front velocity by
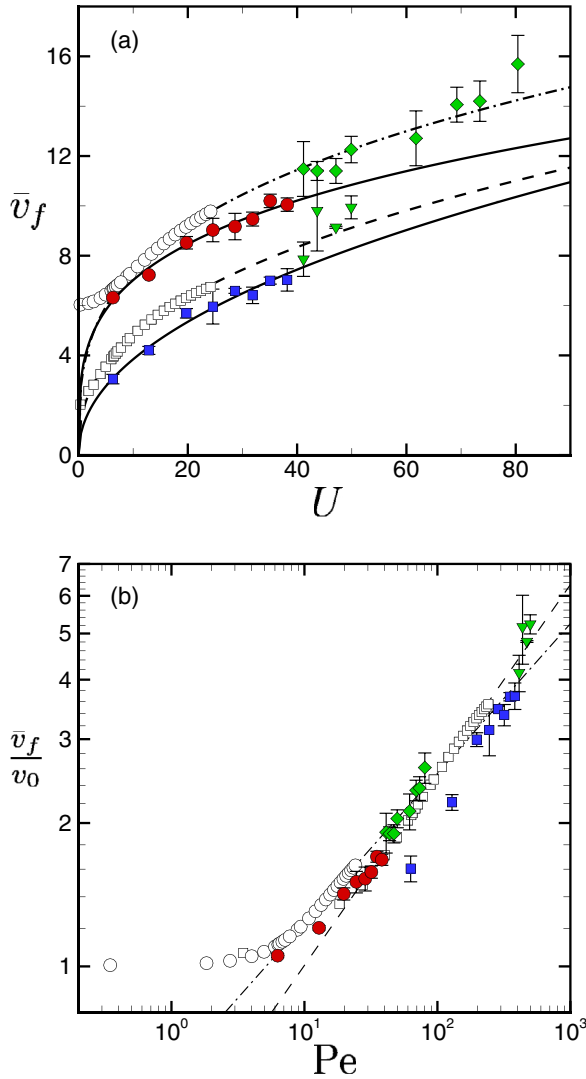
FIG. 25. The variation of the asymptotic front velocity $\bar{v}_f$ with the characteristic velocity $U$ of the underlying flow field. Open symbols are for fronts traveling through straight-parallel convection rolls in the rectangular domain (cf. Figs. 6 and 7). Filled symbols (red, blue, and green) are for fronts traveling through chaotic flow fields in a large cylindrical domain (cf. Figs. 22 and 23). For the chaotic flow field results, each data point is the average of three numerical simulations where the standard deviation about the mean value is shown as the error bars. Circles and diamonds are for Le = 1 and squares and triangles are for Le = 0.1. The diamonds and triangles (green) indicate flow fields that exhibit the oscillatory instability. The solid and dashed lines are power-law curve fits that are described in the text. (a) The front velocity $\bar{v}_f$ versus the characteristic fluid velocity $U$. (b) The same data plotted as the normalized front velocity versus the Péclet number Pe.

changing the orientation of the convection rolls relative to the radial front velocity.

However, there is a significant increase in the front velocity at the onset of the oscillatory instability as shown by the diamonds. The velocity of the front in the weakly turbulent flow eventually surpasses that of the extrapolated value for the straight-parallel rolls for $U \gtrsim 80$ (Ra $\gtrsim 25\,000$). The oscillatory instability results in making the front geometry

TABLE I. The scaling exponents $\alpha_f$ for several cases where $\bar{v}_f \propto U^{\alpha_f}$. These four cases are shown as the power-law curve fits in Fig. 25.

| Le | Cellular flow $\alpha_f$ | Chaotic flow $\alpha_f$ |
|---|---|---|
| 1 | 0.31 | 0.27 |
| 0.1 | 0.40 | 0.48 |

much more complex and wrinkled which we explore further in Sec. III B.

Similar trends are found for Le = 0.1 which are shown using the squares and triangles. The solid line through the squares (blue) is a power-law curve fit of the form $\bar{v}_f = 1.29U^{0.48}$. Again, the presence of spiral defect chaos slows down the front when compared with a front traveling through straight-parallel convection rolls with $\langle \phi \rangle = 0$. However, in this case, the front velocity is more sensitive to the onset of the oscillatory instability and the front velocity in the chaotic flow field surpasses the extrapolated value for $U \gtrsim 50$ (Ra $\gtrsim 13\,000$). The dashed line is the power-law curve fit for the results of a front propagating through straight-parallel convection rolls where $\bar{v}_f \propto U^{0.4}$.

In order to quantify the influence of the roll orientation, relative to the radial front propagation, for the chaotic flow fields we again compute the variation of the front velocity with the reaction zone angle $\phi$. For these disordered flow fields, quantifying the reaction zone angle is more complicated than for the case of the straight and parallel rolls shown in Fig. 17.

For the chaotic flow fields, we use the local wave vector $\vec{q}(x, y, t) = (q_x, q_y)$ to determine the local roll orientation. The local wave vector is evaluated at the horizontal midplane where $q_x$ and $q_y$ are the components of the wave vector in the $x$ and $y$ directions, respectively. It is computed using spatial derivatives of the temperature field $T(x, y, z = 1/2, t)$ as described by Egolf et al. [58]. The basic idea of the local wave vector diagnostic is the assumption of a sinusoidally varying temperature field composing the convection rolls that may be time varying and may have a complicated distribution in space. The result is a vector $\vec{q}$ that yields spatially localized information about the pattern of convection rolls.

From the local wave vector it is straightforward to define a local orientation field for the convection rolls $\theta_l(x, y, t)$ using $\theta_l = \tan^{-1}(q_y/q_x)$ where $\theta_l$ is defined to be over the range $0 \leqslant \theta_l \leqslant \pi$. At any time $t$ we identify the location of the radially propagating reaction zone as the region where $0.1 \leqslant c \leqslant 0.9$. At the spatial regions identified to contain the reaction zone, we also compute the local orientation of the underlying convection rolls. The reaction zone angle $\phi$ is then defined at these regions to be

$$\phi = \begin{cases} \min(\tilde{\theta}, |\pi - \tilde{\theta}|) & \text{for } 0 \leqslant \theta \leqslant \pi, \\ \min(|\pi - \tilde{\theta}|, |2\pi - \tilde{\theta}|) & \text{for } \pi < \theta \leqslant 2\pi, \end{cases} \quad (12)$$

where $\tilde{\theta} = |\theta - \theta_l|$. Using Eq. (12) the reaction zone angle is over the range $0 \leqslant \phi \leqslant \pi/2$.

The spatial variation of the reaction zone angle $\phi$ for fronts traveling through chaotic flow is shown in Fig. 26. The color contours are of $\phi$ computed using Eq. (12) and the black lines indicate the pattern of convection rolls.
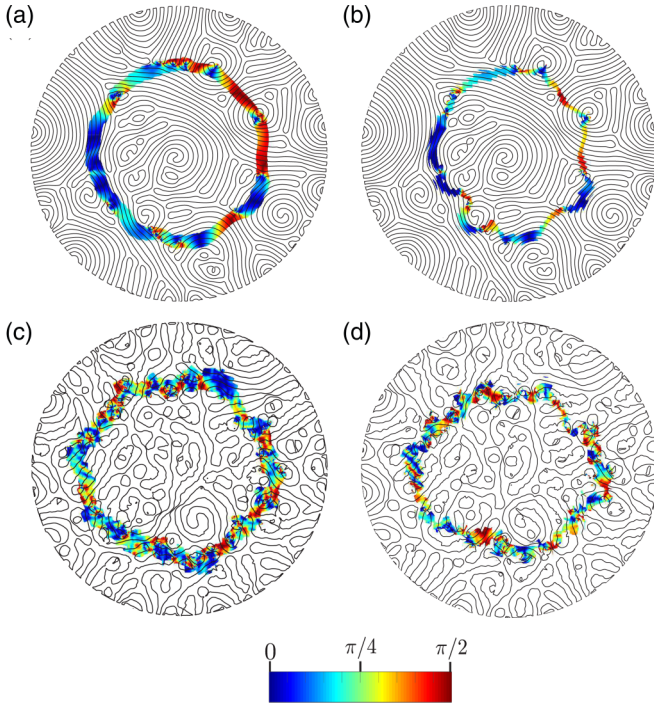
(a) (b)

(c) (d)

$0 \quad \pi/4 \quad \pi/2$

FIG. 26. The spatial variation of the reaction zone angle $\phi$ for fronts traveling through chaotic convection rolls. Color contours are of $\phi$ and the black lines indicate the underlying pattern of convection rolls. The reaction zone angle is computed over the region where the concentration is within the range $0.1 \leqslant c \leqslant 0.9$. The top row is for Ra = 3000 where (a) Le = 1 and (b) Le = 0.1. The bottom row is for Ra = 9000 where (c) Le = 1 and (d) Le = 0.1.
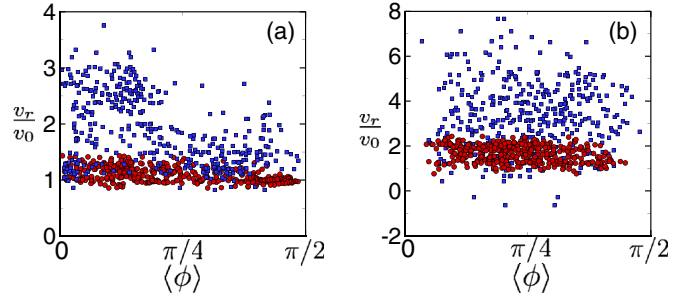


FIG. 27. The variation of the instantaneous scaled radial front velocity $v_r(t)/v_0$ with the radially averaged reaction zone angle $\langle\phi\rangle$ for a chaotic flow field where the circles (red) are for Le = 1 and the squares (blue) are for Le = 0.1. (a) Ra = 3000, (b) Ra = 9000.

Figures 26(a) and 26(b) are for a chaotic flow field with Ra = 3000. In this case, the flow field pattern contains patches of straight and curved convection rolls that are disordered in space. There are also some defect structures in the flow field such as dislocations, wall foci, grain boundaries, and spiral structures.

Figure 26(a) is for Le = 1 which shows that the reaction zone is thick in the radial direction and overall quite annular in shape. In addition, the reaction zone angle varies rather smoothly in the radial and azimuthal directions. Figure 26(b) shows a front for the same flow conditions but where Le = 0.1. In this case, the reaction zone is thinner, its overall shape is more complicated, and there is more azimuthal variation of the reaction zone angle.

Figures 26(c) and 26(d) show the variation of the reaction zone angle for a more chaotic flow field where Ra = 9000 for Le = 1 and 0.1, respectively. The flow field is now significantly more disordered with fewer regions of parallel roll patches and many more defect structures. The spatial variation of the reaction zone angle is now much more complex both in the radial and azimuthal directions.

These spatial variations of the reaction zone angle are probed further in Fig. 27 which shows the variation of the reduced radial front velocity $v_r/v_0$ with the radially averaged reaction zone angle $\langle\phi\rangle$. Results are shown for chaotic convection where Fig. 27(a) is for Ra = 3000 and Fig. 27(b) is for Ra = 9000 using circles (red) for Le = 1 and squares (blue) for Le = 0.1. The data indicate a significant amount of scatter.

Overall, the variation in the data is much larger for Le = 0.1 as expected since the flow field has a stronger influence. In fact, for Le = 0.1 in Fig. 27(b) there are several instances where $v_r < 0$, indicating a local fluctuation in the front velocity back towards the center of the domain.

Figure 27(a) indicates the weak trend where the magnitude of the front velocity decreases with increasing reaction zone angle. This suggests a weak dependence of the front velocity on the reaction zone angle for this flow field. This trend is in agreement with the results shown in Fig. 18 for straight-parallel convection rolls.

In Fig. 27(b), however, there is no clear trend in the data as a function of the reaction zone angle as shown by the relatively uniformly scattered distribution of the data points. These results suggest that the reaction zone angle is not related in a significant way to the front velocity. This is reasonable for this flow field which is much more disordered where patches of parallel rolls are not common and the role of defects is more important.

The absence of front velocity values near $\langle\phi\rangle \approx 0$ and $\langle\phi\rangle \approx \pi/2$ in Fig. 27(b) are the result of the significant variations of $\phi$ in the radial direction. This causes the radial average $\langle\phi\rangle$ to have values away from these bounds. For example, a value of $\langle\phi\rangle = \pi/2$ would require $\phi = \pi/2$ over the entire radial slice across the front at that value of $\theta$. It is apparent in Figs. 26(c) and 26(d) that this does not occur. However, in Figs. 26(a) and 26(b) this does occur which results in values of $\langle\phi\rangle$ near 0 and $\pi/2$ in Fig. 27(a).

It is interesting that there are values of $v_r$ that are much larger than the rest in Fig. 27. Upon closer inspection, it is found that these local spikes in the front velocity occur in regions where the local fluid velocity is large. Regions that have a large fluid velocity are the result of complex spatial and temporal interactions of the flow field patterns that vary over length scales of several roll widths. As a result, the local topology of the flow field pattern is not sufficient to predict where these large fluid velocities may occur and, as a result, the regions of large fluid velocity may occur anywhere in the flow field including near defect structures and near patches of parallel rolls.

It is important to recall that the propagating fronts represented in Figs. 26 and 27 have asymptotic front velocities $\bar{v}_f$ that are smaller than the front velocity that would occur for a front traveling through a field of straight-parallel convection

rolls with the same value of the characteristic fluid velocity $U$ and with a reaction zone angle of zero (see Fig. 25). For example, for the Le = 1 results (circles) in Fig. 27(b), the asymptotic front velocity in the chaotic flow field is $\bar{v}_f/v_0 = 1.68$. This is approximately equal to the average value of all of the circles in Fig. 27(b) since these results are for a particular time in the front evolution toward its asymptotic velocity. Using the power-law scaling result for a front traveling through straight-parallel rolls with the same value of $U$ yields $\bar{v}_f/v_0 = 1.89$. The front velocity through the straight-parallel rolls is larger, on average, than the front traveling through the chaotic flow field. However, there are quite a few instances where the front velocity in the chaotic flow field is locally faster than the asymptotic front velocity through the straight-parallel convection rolls.

The trends are similar for the Le = 0.1 results of Fig. 27(b) where $\bar{v}_f/v_0 = 3.70$ for a front traveling through the chaotic flow field and $\bar{v}_f/v_0 = 4.32$ for a front traveling through straight-parallel convection rolls with the same value of $U$. In this case, the fluctuations in the front velocity are even larger for the front in the chaotic flow.

Overall, these results suggest the presence of two competing mechanics that affect the front velocity in these disordered flows. These are the local convection roll orientation and the geometry of the reaction zone between the reactants and the products. These are competing because reaction zone angles away from zero *slow down* the front whereas the increased complexity of the reaction zone is expected to *increase* the front velocity.

For the weakly chaotic flow fields, such as the results for Ra = 3000, the flow has effectively shuffled the orientation of the convection rolls relative to the radially propagating front. As a result, the propagating front is now faced with convection rolls of many different orientations as it propagates outward. The resulting front velocity, as a result, is less than it would be for the optimum case of a reaction zone angle of zero through straight-parallel convection rolls.

However, the flow fields of Fig. 21 are more complex than fields of convection rolls at different orientations through the defect structures and time dependence. These effects cause the scatter in Fig. 27 as opposed to the much smoother trends shown in Fig. 18.

As the Rayleigh number increases, the spatial structure of the flow field becomes more complicated. The number of defects increases significantly and the area covered by patches of parallel convection rolls decreases. As a result, the influence of roll orientation decreases and the influence of the complex flow field increases. This results in the more uniformly distributed values of the front velocity with reaction zone angle in Fig. 27(b). However, the interface of the front geometry is now more complex. The front velocity is expected to increase as the interface between the reactants and products increases.

### B. Geometry of the front

We next explore the complex geometry of the propagating fronts in the chaotic and weakly turbulent flow fields. Our approach is to use the level-set where the concentration field is $c = \frac{1}{2}$ at the horizontal midplane $z = \frac{1}{2}$ to identify and locate
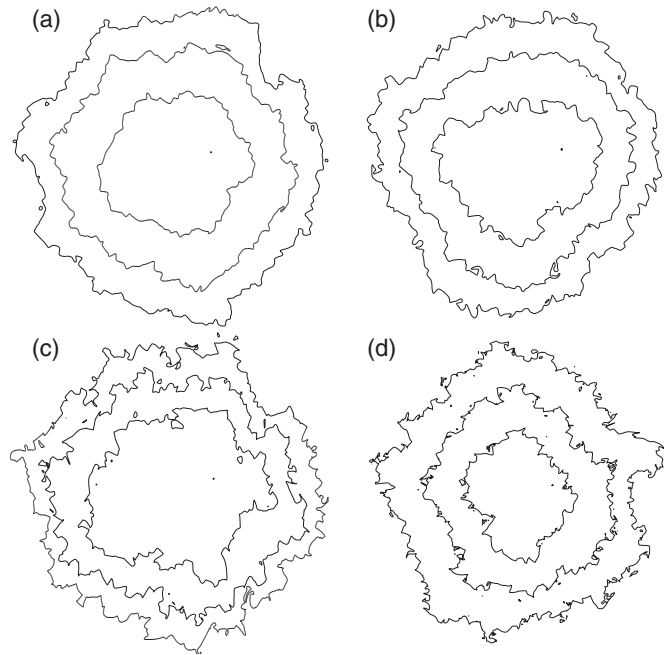


FIG. 28. The geometry of propagating fronts in chaotic flow fields. The top row is for Le = 1 where (a) Ra = 9000 and (b) Ra = 25 000. The bottom row is for Le = 0.1 where (c) Ra = 9000 and (d) Ra = 13 000. The front is shown at the horizontal midplane using a black contour of the level set $c(x, y, z = \frac{1}{2}) = \frac{1}{2}$. For each panel the front is shown for three different instances of time which appear as the three separate concentric objects. The front is shown at the following times: (a) $t = 2, 3, 3.7$; (b) $t = 1.5, 2, 2.4$; (c) $t = 3, 4, 4.7$; (d) $t = 2, 3, 4$.

the front. Images illustrating the front geometry found in this manner are shown in Fig. 28 for several chaotic flow fields. The top row is for Le = 1 where (a) Ra = 9000 and (b) Ra = 25 000. The bottom row shows fronts for Le = 0.1 where (c) Ra = 9000 and (d) Ra = 13 000. The front is colored black and white indicates the absence of the front. In each panel of Fig. 28 the front is shown at three different instances of time to illustrate its variation as it propagates from the center of the domain outward. It is clear that the front is quite complicated in structure and varies spatially and includes noncontiguous pieces which appear as small isolated black regions.

By inspection of Fig. 28 it is clear that the fronts appear more geometrically complex for Le = 0.1. This is evident by comparing Figs. 28(a)–28(c) where Ra = 9000 and the only difference between the two results is the value of the Lewis number.

In order to quantify the complexity of the front geometry, as defined using the approach to generate the images of Fig. 28, we will use the box counting dimension $D_b$ [59]. The box counting dimension is advantageous for our purposes because it can be applied to complex, and not necessarily self-similar, geometries in two and three dimensions. Many natural examples exist of objects that yield fractional values of the box counting dimension including fluid turbulence, complex networks of blood vessels in the human body, cracking structures in a solid and the shapes of clouds, coastlines, and mountains, to name a few [60].
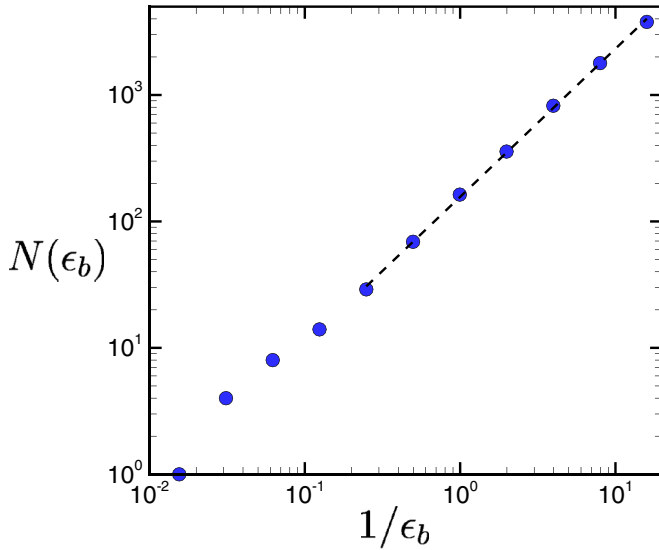
FIG. 29. The variation of $N(\epsilon_b)$ with $\epsilon_b$ for a front propagating in a chaotic flow field with Ra = 13 000 and Le = 0.1 at a time $t = 3.6$ since the initiation of the front. The dashed line is a curve fit through the points which yields a box counting dimension of $D_b(t) = 1.15$ using Eq. (13).



FIG. 30. (a) The variation of the box counting dimension $D_b$ with time $t$ using the front located at the horizontal midplane where $z = \frac{1}{2}$. The dashed line is the time averaged value of $\langle D_b \rangle_t = 1.15$. The root-mean-squared value of the fluctuations about the mean value is 0.02. (b) The variation of $D_b$ with the vertical coordinate $z$. Results are shown for three different times after the front has reached a steady front velocity where circles (blue) $t = 2.0$, triangles (green) $t = 2.5$, and squares (red) $t = 3.0$. For the results Ra = 13 000, Le = 0.1, and images of the front are shown in Fig. 28(d).

The essential idea is to compute the minimum number of boxes $N(\epsilon_b)$ of size $\epsilon_b$ that are required to cover the geometrical object in question where features smaller than $\epsilon_b$ are ignored. Using this approach for different values of $\epsilon_b$ one then determines how $N(\epsilon_b)$ scales with $\epsilon_b$ as $\epsilon_b \to 0$. If this limit exists, the box counting dimension is given by

$$D_b = \lim_{\epsilon_b \to 0} \frac{\ln N(\epsilon_b)}{\ln(1/\epsilon_b)}. \tag{13}$$

In practice, we compute $N(\epsilon_b)$ over the range of numerically accessible values of $\epsilon_b$ and use $\ln N(\epsilon_b) \propto \ln(1/\epsilon_b)$ to determine if $D_b$ has converged to a value for our smallest values of $\epsilon_b$. We have conducted many tests using our numerical approach to ensure that our computations yield the expected result for well known examples such as Euclidean areas, volumes, and various fractals such as the von Koch curve.

In all of our spectral element numerical simulations of propagating fronts in chaotic flow fields we have used 3072 hexahedral spectral elements with 16th order Gauss-Lobatto-Legendre polynomials. In essence, this yields that the smallest spatial feature that can be resolved in our computations has a length scale of approximately 0.08. Therefore, the smallest box size we use is $\epsilon_b \approx 0.08$ in our computations of the box counting dimension.

Figure 29 provides an example of the results generated using this approach for a front propagating in a chaotic flow field where Ra = 13 000 and Le = 0.1 [see Fig. 28(c)]. In this figure we have plotted the variation of $N(\epsilon_b)$ with $\epsilon_b^{-1}$ on a log scale. As the value of $\epsilon_b$ decreases, the results approach the straight dashed line. The slope of this line provides the value of $D_b(t)$ which for these results is $D_b(t) = 1.15$. We then compute the time variation of the box counting dimension of the front as it propagates outward toward the sidewalls.

We have found that $D_b(t)$ quickly approaches a steady value, on average, with small fluctuations about this mean
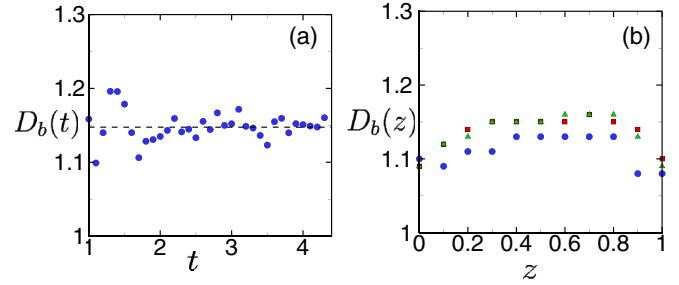
value. This example is typical of all of our calculations of $D_b(t)$. In Fig. 30 we show an example that demonstrates this trend for the case of Ra = 13 000 and Le = 0.1 which represents the most complex front we have explored here. Figure 30(a) shows the time variation of the box counting dimension using the front that has been identified at the horizontal midplane $z = \frac{1}{2}$. The front is located as the $c = \frac{1}{2}$ level set as shown in Fig. 28(d). The box counting dimension $D_b(t)$ fluctuates about its mean value of $\langle D_b \rangle = 1.15$ which is represented as the dashed line. The fluctuations about the mean have root-mean-squared value of 0.02.

In Fig. 30(b) we show the variation of the box counting dimension with the value of $z$ that is used to determine the location of the front. Results are presented for three different times during the front propagation where the front velocity has reached a steady value where circles (blue) are for $t = 2$, triangles (green) are for $t = 2.5$, and squares (red) are for $t = 3.0$. We have computed the box counting dimension at 11 equally spaced values of $z$ over the range of $0 \leqslant z \leqslant 1$. The results indicate only a weak dependence on the value of $D_b$ with the value of $z$ used to determine location of the front. The front is actually the two-dimensional ribbon structure shown in Fig. 24, however, these results indicate that it is possible to estimate the box counting dimension of the front using only the slice of the front located at the midplane. This greatly reduces the amount of computations required to compute the box counting dimension of the fronts and we will use this approach in our analysis that follows.

We have computed the box counting dimension of all of the fronts in the chaotic and weakly turbulent fluid flows that we have discussed. Figure 31 shows the variation of $\bar{D}_b$ with the reduced Rayleigh number $\epsilon$. We define $\bar{D}_b$ using

$$\bar{D}_b = \langle D_b \rangle_t - 1 \tag{14}$$

as a measure of the long-time average complexity of the front geometry. The term $\langle D_b \rangle_t$ is the long-time average value of $D_b(t)$. The circles (red) and the diamonds (green) are the results for Le = 1 and the squares (blue) and triangles (green) are for Le = 0.1. The diamonds and triangles (green) are for
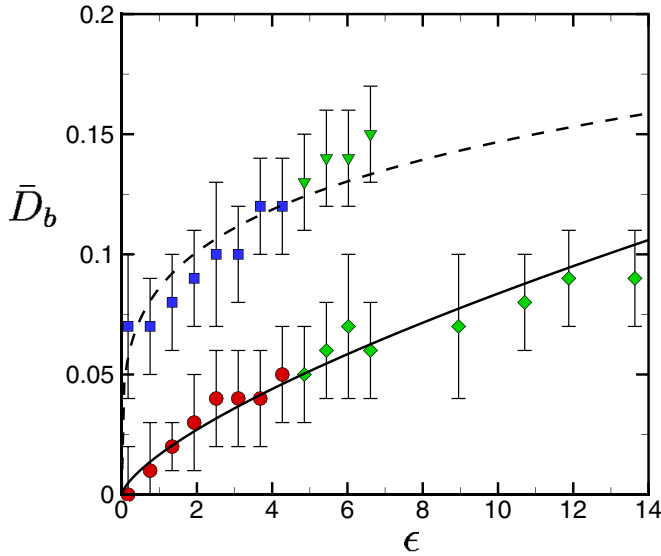
FIG. 31. The variation of the reduced box counting dimension $\bar{D}_b$ with the reduced Rayleigh number $\epsilon$. The squares (blue) and triangles (green) are for Le $= 0.1$ and the circles (red) and diamonds (green) are for Le $= 1$. Errors bars are included which represent the standard deviation about the mean value. The solid and dashed lines are power-law curve fits through the data where $\bar{D}_b = 0.02\epsilon^{0.7}$ and $\bar{D}_b = 0.08\epsilon^{0.23}$, respectively. An oscillatory instability is present for $\epsilon \gtrsim 4.85$ which is indicated as the triangles and diamonds (green).

the weakly turbulent flows where the value of $\epsilon$ is above the threshold for the oscillatory instability. The error bars are the standard deviation of the dimension about its mean value. The variation of the dimension with the reduced Rayleigh number is described by the power-law scaling $\bar{D}_b \propto \epsilon^{\alpha_b}$ where the scaling exponent is $\alpha_b \approx 0.7$ for Le $= 1$ and $\alpha_b \approx 0.2$ for Le $= 0.1$. The curve fits are shown as the solid and dashed lines.

It is clear that the box counting dimension exhibits an increasing trend with increasing $\epsilon$. This is expected since the flow field becomes more complex with $\epsilon$. Also, $\bar{D}_b$ for Le $= 0.1$ is always larger than $\bar{D}_b$ for Le $= 1$. This indicates that the stronger influence of the flow field for a smaller Lewis number translates into a more geometrically complex front.

For both the Le $= 1$ and $0.1$ results, the asymptotic front velocities $\bar{v}_f$ for the three largest values of $\epsilon$ shown in Fig. 31 exceed the front velocity through straight and parallel convection rolls with a reaction zone angle of zero. Figure 31 suggests that this front velocity enhancement is due, at least in part, to the increased complexity of the front geometry.

This enhancement to the front velocity is expected to increase as $\epsilon$ is increased further. However, using our results it is unclear if the power-law curve fits continue to be useful for much larger values of $\epsilon$ since the flow field characteristics are expected to change significantly as turbulence is approached. This would be interesting to pursue, however, we have not explored this limit further.

It is interesting to compare our results with the results in the literature that find fractal dimensions of $D_f = \frac{7}{3}$ for a wide range of conditions and flow fields [4,18,33,34]. A value of

$D_f = \frac{7}{3}$ would be equivalent to $\bar{D}_b = \frac{1}{3}$ using our notation. There is an increasing trend in our results that does not appear to be approaching a steady value for large $\epsilon$. Although it is possible that our results may also approach a value of $\frac{1}{3}$ at larger $\epsilon$, we are not able to make any quantitative predictions using our present results and this interesting question remains open.

## IV. CONCLUSIONS

We have studied the velocity and geometry of propagating pulled fronts traveling through a range of convective flow fields. Using large-scale computations, we have done this for an experimentally accessible flow field using a FKPP nonlinearity for the reaction. We have focused upon fronts with a finite reaction zone thickness and finite speed which align well with the types of fronts that are often found in nature and in experiment. Using this approach, we have provided physical insights into the dynamics of fronts for conditions beyond the reach of current theoretical descriptions.

Our results do not fall into the well understood limiting cases of Da $\gg 1$ or Da $\ll 1$ where Pe $\gg 1$ and DaPe $\gg 1$. However, our results still yield power-law scalings for the asymptotic front velocity as a function of the characteristic fluid velocity for both cellular and chaotic flow. For Le $= 1$ we find that the scaling exponent is roughly unchanged when considering cellular or chaotic flow where $\alpha_f \approx 0.3$. On the other hand, for Le $= 0.1$ where the advection is more important, we find that the scaling exponent is larger for chaotic flow where its value is $\alpha_f \approx 0.5$. Furthermore, we have quantified the variation of the front velocity as a function of the convection roll orientation relative to the direction of the propagating front.

We have found that weakly chaotic fluid motion can slow down a propagating front, on average, when compared to the front velocity through a cellular flow with the same characteristic fluid velocity. However, with the onset of the oscillatory instability the front velocity in a weakly turbulent flow eventually overtakes the front velocity in the equivalent cellular flow. Our results suggest that this increase in front velocity is due to the wrinkling of the front interface due to the fluid motion. We have found that the front geometry is fractal for chaotic and weakly turbulent flow and that its dimension increases with increasing values of the Rayleigh number.

Our numerical approach is quite general and it would be interesting to explore a number of situations. This includes the dynamics of pushed fronts, more sophisticated models for the nonlinear reaction, the role of back-action, and higher Rayleigh number flows in order to study the propagation of fronts as turbulence is approached.

[1] W. van Saarloos, Front propagation into unstable states, Phys. Rep. **386**, 29 (2003).

[2] J. Xin, Front propagation in heterogeneous media, SIAM Rev. **42**, 161 (2000).

[3] F. A. Williams, *Combustion Theory* (Benjamin-Cummings, Menlo Park, CA, 1985).

[4] K. R. Sreenivasan, R. Ramshankar, and C. Meneveau, Mixing, entrainment, and fractal dimensions of surfaces in turbulent flows, Proc. R. Soc. London, Ser. A **421**, 79 (1989).

[5] N. Vladimirova, P. Constantin, A. Kiselev, O. Ruchayskiy, and L. Ryzhik, Flame enhancement and quenching in fluid flows, Combust. Theory Modell. **7**, 487 (2003).

[6] J. H. Chen, E. R. Hawkes, R. Sankaran, S. D. Mason, and H. G. Im, Direct numerical simulations of ignition front propagation in a constant volume with temperature inhomogeneities I. Fundamental analysis and diagnostics, Combust. Flame **145**, 128 (2006).

[7] V. A. Sabelnikov and A. N. Lipatnikov, Transition form pulled to pushed fronts in premixed turbulent combustion: Theoretical and numerical study, Combust. Flame **162**, 2893 (2015).

[8] J. Ross, S. C. Müller, and C. Vidal, Chemical waves, Science **240**, 460 (1998).

[9] T. Tèl, A. de Moura, C. Grebogi, and G. Károlyi, Chemical and biological activity in open flows: A dynamical system approach, Phys. Rep. **413**, 91 (2005).

[10] S. Gowen and T. H. Solomon, Experimental studies of coherent structures in an advection-reaction-diffusion system, Chaos **25**, 087403 (2015).

[11] M. G. Turner, W. H. Romme, R. H. Garcia, and W. W. Hargrove, Effects of fire size and pattern on early succession in Yellowstone national park, Ecol. Monogr. **67**, 411 (1997).

[12] W. W. Hargrove, R. H. Gardner, M. G. Turner, W. H. Romme, and D. G. Despain, Simulating fire patterns in heterogeneous landscapes, Ecol. Modell. **135**, 243 (2000).

[13] E. Pastor, L. Zárate, E. Planas, and J. Arnaldos, Mathematical models and calculation systems for the study of wildland fire behavior, Prog. Energy Combust. Sci. **29**, 139 (2003).

[14] A. T. Peterson, Predicting the geography of species' invasions via ecological niche modeling, Q. Rev. Biol. **78**, 419 (2003).

[15] M. N. Kuperman and H. S. Wio, Front propagation in epidemiological models with spatial dependence, Phys. A (Amsterdam) **272**, 206 (1999).

[16] C. A. Russell, D. A. Smith, L. A. Waller, J. E. Childs, and L. A. Real, A priori prediction of disease invasion dynamics in a novel environment, Proc. R. Soc. London, Ser. B **271**, 21 (2004).

[17] R. R. Prasad, C. Meneveau, and K. R. Sreenivasan, Multifractal Nature of the Dissipation Field of Passive Scalars in Fully Turbulent Flows, Phys. Rev. Lett. **61**, 74 (1988).

[18] B. D. Haslam and P. D. Ronney, Fractal properties of propagating fronts in a strongly stirred fluid, Phys. Fluids **7**, 1931 (1995).

[19] A. Pocheau and F. Harambat, Front propagation in a laminar cellular flow: shapes, velocities, and least time criterion, Phys. Rev. E **77**, 036304 (2008).

[20] C. O. Mehrvarzi and M. R. Paul, Front propagation in a chaotic flow field, Phys. Rev. E **90**, 012905 (2014).

[21] E. Beauvier, S. Bodea, and A. Pocheau, Front propagation in a regular vortex lattice: Dependence on the vortex structure, Phys. Rev. E **96**, 053109 (2017).

[22] J. Martin, N. Rakotomalala, D. Salin, and M. Böckmann, Buoyancy-driven instability of an autocatalytic reaction in a Hele-Shaw cell, Phys. Rev. E **65**, 051605 (2002).

[23] F. Rossi, M. A. Budroni, N. Marchettini, and J. Carballido-Landeira, Segmented waves in a reaction-diffusion-convection system, Chaos **22**, 037109 (2012).

[24] P. W. Megson, M. L. Najaran, K. E. Lilienthal, and T. H. Solomon, Pinning of reaction fronts by burning invariant manifolds in extended flows, Phys. Fluids **27**, 023601 (2015).

[25] M. Doan, J. J. Simmons, K. E. Lilienthal, T. H. Solomon, and K. A. Mitchell, Barriers to front propagation in laminar, three-dimensional fluid flows, Phys. Rev. E **97**, 033111 (2018).

[26] M. Abel, A. Celani, D. Vergni, and A. Vulpiani, Front propagation in laminar flows, Phys. Rev. E **64**, 046307 (2001).

[27] M. Abel, M. Cencini, D. Vergni, and A. Vulpiani, Front speed enhancement in cellular flows, Chaos **12**, 481 (2002).

[28] M. C. Cross and P. C. Hohenberg, Pattern formation outside of equilibrium, Rev. Mod. Phys. **65**, 851 (1993).

[29] G. L. North and D. A. Santavicca, The fractal nature of premixed turbulent flames, Combust. Sci. Technol. **72**, 215 (1990).

[30] J. R. Mahoney and K. A. Mitchell, Turnstile mecahnism for fronts propagating in fluid flows, Chaos **23**, 043106 (2013).

[31] T. C. Halsey, M. H. Jensen, L. P. Kadanoff, I. Procaccia, and B. I. Shraiman, Fractal measures and their singularities: the characterization of strange sets, Phys. Rev. A **33**, 1141 (1986).

[32] K. R. Sreenivasan, Fractals and multifractals in fluid turbulence, Annu. Rev. Fluid Mech. **23**, 539 (1991).

[33] A. R. Kerstein, Fractal dimension of turbulent premixed flames, Combust. Sci. Technol. **60**, 441 (1988).

[34] R. Ramashankar and J. P. Gollub, Transport by capillary waves. Part II Scalar dispersion and structure of the concentration field, Phys. Fluids A **3**, 1344 (1991).

[35] E. Ott and T. M. Antonsen, Chaotic Fluid Convection and the Fractal Nature of Passive Scalar Gradients, Phys. Rev. Lett. **61**, 2839 (1988).

[36] M. R. Paul, K.-H. Chiam, M. C. Cross, P. F. Fischer, and H. S. Greenside, Pattern formation and dynamics in Rayleigh-Bénard convection: numerical simulations of experimentally realistic geometries, Phys. D (Amsterdam) **184**, 114 (2003).

[37] E. Bodenschatz, W. Pesch, and G. Ahlers, Recent developments in Rayleigh-Bénard convection, Annu. Rev. Fluid Mech. **32**, 709 (2000).

[38] J. R. de Bruyn, E. Bodenschatz, S. W. Morris, D. S. Cannell, and G. Ahlers, Apparatus for the study of Rayleigh-Bénard convection in gases under pressure, Rev. Sci. Instrum. **67**, 2043 (1996).

[39] A. N. Kolmogorov, I. G. Petrovskii, and N. S. Piskunov, A study of the equation of diffusion with increase in the quantity of matter, and its application to a biological problem, Moscow Univ. Math. Bull. **1**, 1 (1937).

[40] R. A. Fischer, The wave of advance of advantageous genes, Proc. Annu. Symp. Eugen. Soc. **7**, 355 (1937).

[41] http://nek5000.mcs.anl.gov

[42] P. F. Fischer, An overlapping Schwarz method for spectral element solution of the incompressible Navier-Stokes equations, J. Comput. Phys. **133**, 84 (1997).

[43] K.-H. Chiam, M. R. Paul, M. C. Cross, and H. S. Greenside, Mean flow and spiral defect chaos in Rayleigh-Bénard convection, Phys. Rev. E **67**, 056206 (2003).

[44] P. Constantin, A. Kiselev, A. Oberman, and L. Ryzhik, Bulk burning rate in passive-reactive diffusion, Arch. Ration. Mech. Anal. **154**, 53 (2000).

[45] U. Ebert and W. van Saarloos, Front propagation in unstable states: universal algebraic convergence towards uniformly translating pulled fronts, Phys. D (Amsterdam) **146**, 1 (2000).

[46] P. Clavin and F. A. Williams, Theory of premixed-flame propagation in large-scale turbulence, J. Fluid Mech. **90**, 589 (1979).

[47] Y. Pomeau, Dispersion dans un écoulement en présence de zones de recirculation, C. R. Acad. Sci. **301**, 1323 (1985).

[48] B. Shraiman, Diffusive transport in a Rayleigh-Bénard convection cell, Phys. Rev. A **36**, 261 (1987).

[49] M. N. Rosenbluth, H. L. Berk, I. Doxas, and W. Horton, Effective diffusion in laminar convective flow, Phys. Fluids **30**, 2636 (1987).

[50] B. Audoly, H. Beresytcki, and Y. Pomeau, Réaction diffusion en écoulement stationnaire rapide, C. R. Acad. Sci., Ser. IIb: Mec., Phys. Chim., Astron. **328**, 255 (2000).

[51] M. R. Paul, M. I. Einarsson, P. F. Fischer, and M. C. Cross, Extensive chaos in Rayleigh-Bénard convection, Phys. Rev. E **75**, 045203 (2007).

[52] A. Karimi and M. R. Paul, Quantifying spatiotemporal chaos in Rayleigh-Bénard convection, Phys. Rev. E **85**, 046201 (2012).

[53] J. L. Kaplan and J. A. Yorke, Lect. Notes Math. **730**, 204 (1979).

[54] S. W. Morris, E. Bodenschatz, D. S. Cannell, and G. Ahlers, Spiral Defect Chaos in Large Aspect Ratio Rayleigh-Bénard Convection, Phys. Rev. Lett. **71**, 2026 (1993).

[55] F. H. Busse, The oscillatory instability of convection rolls in a low Prandtl number fluid, J. Fluid Mech. **52**, 97 (1972).

[56] P. F. Fischer and J. Mullen, Filter-based stabilization of spectral element methods, C. R. Acad. Sci. Paris, Ser. I: Math **332**, 265 (2001).

[57] K.-H. Chiam, M. C. Cross, H. S. Greenside, and P. F. Fischer, Enhanced tracer transport by the spiral defect chaos state of a convecting fluid, Phys. Rev. E **71**, 036205 (2005).

[58] D. A. Egolf, I. V. Melnikov, and E. Bodenschatz, Importance of Local Pattern Properties in Spiral Defect Chaos, Phys. Rev. Lett. **80**, 3228 (1998).

[59] J. D. Farmer, E. Ott, and J. A. Yorke, The dimension of chaotic attractors, Phys. D (Amsterdam) **7**, 153 (1983).

[60] H. Peitgen, H. Jürgens, and D. Saupe, *Chaos and Fractals* (Springer, Berlin, 2004).